Posture Dependent Dynamics in Robotic Machining

by

Hamed Assadi
B.Sc., Isfahan University of Technology, 2016

A Thesis Submitted in Partial Fulfillment of the
Requirements for the Degree of

Master of Applied Science

in the Department of Mechanical Engineering

Posture Dependent Dynamics in Robotic Machining

by

Hamed Assadi
B.Sc., Isfahan University of Technology, 2016

Supervisory Committee

Dr. Keivan Ahmadi, Supervisor
(Department of Mechanical Engineering)

Dr. Brad Buckham, Departmental Member
(Department of Mechanical Engineering)

Supervisory Committee

Dr. Keivan Ahmadi, Supervisor
(Department of Mechanical Engineering)

Dr. Brad Buckham, Departmental Member
(Department of Mechanical Engineering)

Abstract

Compared to conventional machine tools, industrial robots offer great advantages such as multitasking, larger workspace, and lower price. However, these advantages of robots are undermined by their high structural flexibility leading to excessive deflections, severe vibrations, and ultimately violating dimensional tolerances and poor surface finish. Modeling the dynamics of robots under machining (e.g. milling and drilling) forces is essential for reducing deflections and vibrations during the process. Although modeling the dynamics of traditional machining systems is a well-studied subject, the existing modeling approaches are not applicable to robotic manipulators because of the posture-dependent dynamics of industrial robots. Within this context, the presented thesis aims to predict the stability of vibrations during robotic machining operations through prediction of posture dependent dynamic behavior of robots.

A rigid-body modeling approach is used to identify the dynamic parameters of the robotic manipulator based on least squares estimation method. Next, by adopting a rigid link flexible joint model and employing experimental modal analysis to identify the joint stiffness and damping parameters, posture dependent dynamic response prediction of the robot is achieved. Finally, the posture-dependent milling stability is presented as a function of the predicted tool center point transfer function, spindle speed, and axial depth of cut. A Staubli TX200 robot and a Kuka KR90 robot are used as experimental case studies.

Contents

List of Tables

List of Figures

Acknowledgments

The author is thankful to **Mr. Hoai Nam Huynh** for performing experimental measurements of this work. The identification of the KUKA KR90 robot was also performed collaboratively with Mr. Huynh during his visit of University of Victoria.

The funding for this research was provided by the Natural Sciences and Engineering Research Council of Canada (NSERC) under Discovery Grant program.

Dedication

I would like to dedicate this thesis to my loving parents.

Chapter 1

Introduction

1.1 Robotic Machining

Industrial robots are used to perform a wide range of tasks in automated manufacturing systems. For instance, they are used for assembly[66], welding[25], and painting[75] in the production lines. Figure 1.1 presents three application examples of industrial robots.

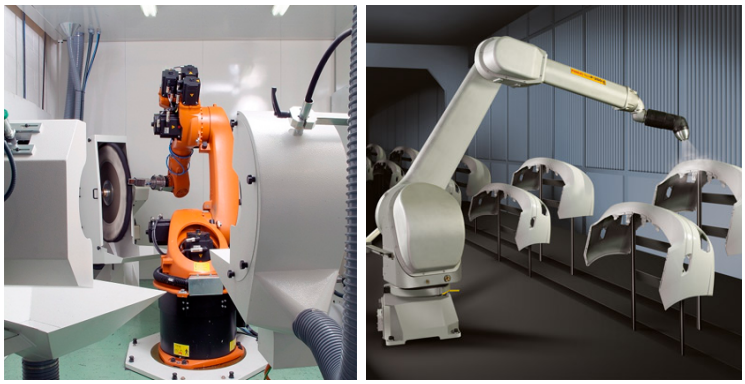

(a) (b)

(c)

Figure 1.1: Examples of industrial robot applications (a) Polishing robot[89] (b) Painting robot[87] (c) Welding robot[90]

There has been a growing interest in using industrial robots for material removal processes, such as deburring[39] and polishing[33]. Table 1.1 presents a few products from various industrial sectors that include some type of robotic machining in their manufacturing processes.

Table 1.1: A few of robotic machining applications[22]

End user segment	Process	Product
All segments	Milling	Rapid prototyping
Aerospace	Grinding, polishing, drilling, cutting	Turbine blades, bulkheads, insulation,wing segments
Automotive	De-flashing, grinding, drilling, milling, cutting	Engines, truck frames, body panels,door knobs, bumpers, stamping dies, sand cores
Fashion	Milling, sanding	Mannequin molds, mannequins
Foundries	De-burring, milling, drilling, routing, finishing	Molds, castings
Marine	Milling	Boat hauls
Medical	Grinding, polishing	Prosthesis
Entertainment Ind.	Milling	Move set props, amusement park scenery
Plastics	Milling, routing	Molds, helmets
Woodworking	Milling, routing	Hot-tub molds, furniture, trim, banisters, modeling board

Compared to the conventional machine tools, industrial robots have many advantages, such as: lower capital investment, larger workspace, and the ability to perform various tasks using one robot. Though, these remarkable advantages come at the cost of low structural flexibility of the system compared to Computer Numerical Controlled (CNC) machines. For the open-loop serial articulated robots, which are widely used in industrial applications (E.g.

Figure 1.1a), this problem is more intense due to the serial structure of the system and error accumulation. For the sake of comparison, 1N force applied at the Tool Centre Point (TCP) of a typical robotic milling system will cause $1\mu m$ deflection, but it will cause only $0.02\mu m$ at the tip of the tool mounted on a typical CNC machine tool[61]. The lower structural rigidity in industrial robots compared to CNC machine tools results in extreme tool vibrations, due to the presence of large periodic machining forces, which can lead to severe damages to the work-piece and the robot[38].

1.2 Machining stability

Uncontrolled vibrations during machining process can lead to poor surface finish, rapid tool wear and breakage, low productivity[23], or even damaged spindle. Machining vibrations can be classified in to two main categories: forced vibrations, due to periodic machining forces [92], and unstable self-excited vibrations, due to the instability of the dynamics of the machining system, also known as chatter[57].

Regenerative chatter is unstable self-excited vibrations that develop due to the feedback between vibrations generated in subsequent cuts in machining[82]. The cutting forces are proportional to the uncut chip thickness (h) (See Figure 4.14), which comprises the feed per revolution of the tool (h_0), modulated by the phase delay between the vibration waves generated by the current tooth ($r(t)$) and the previous tooth ($r(t-\tau)$). As a result, the overall response of the tool includes the steady state forced vibrations, due to h_0, and self-excited vibrations due to $\Delta r(t) = r(t) - r(t-\tau)$. The dynamics of self-excited vibrations of the tool can be described using the closed loop system shown in Figure 4.15, which may become unstable if inappropriate spindle speed and depth of cut are used. Studying the stability of this closed loop system results in generation of the stability lobe diagrams, describing the maximum axial depth of cut that can be used at each spindle speed before vibrations become unstable. Figure 1.2 presents a generic stability lobe diagram. Below the stability limits, the self-exciting vibrations will be damped out, which results in stable machining condition, and anywhere above this limit describes the unstable machining conditions.

While modeling and avoidance of regenerative chatter in machine tools is a well-studied topic [8, 6, 81], chatter in robotic milling has gained attention only in recent years[19, 35, 50, 58, 62, 85].

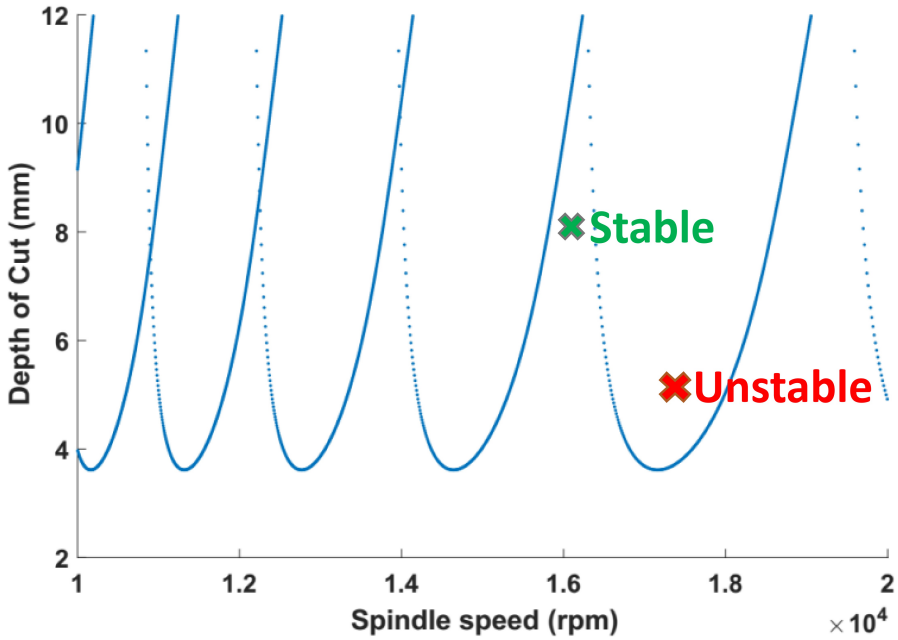

Figure 1.2: Generic form of milling stability lobe diagram.

1.3 Varying dynamics in robots

The application of the available machine tool vibration models to studying robotic milling is restricted due to the fundamental differences between the dynamics of articulated robotic manipulators and CNC machine tools. The main difference between an articulated robot and a conventional machine tool is the use of flexible rotational joints in robots instead of highly rigid linear transmission systems used in CNC machines. In addition to low structural flexibility, which was discussed previously, this results in varying dynamics of robot TCP in Cartesian space, while conventional machine tools offer almost constant dynamics through their work-space. Posture dependency of robot dynamics is demonstrated in Figure 1.3, where direct Frequency Response Functions (FRFs) of a KUKA R2500 robot were measured at TCP in x and y directions for two different postures. As shown in this figure, high frequency modes (¿500Hz) that are mainly associated with the deflections of the small parts of the robot and spindle do not vary by changing the posture; however, low frequency modes, that describe the motion of the heavier links of the robot, vary in different robot postures.

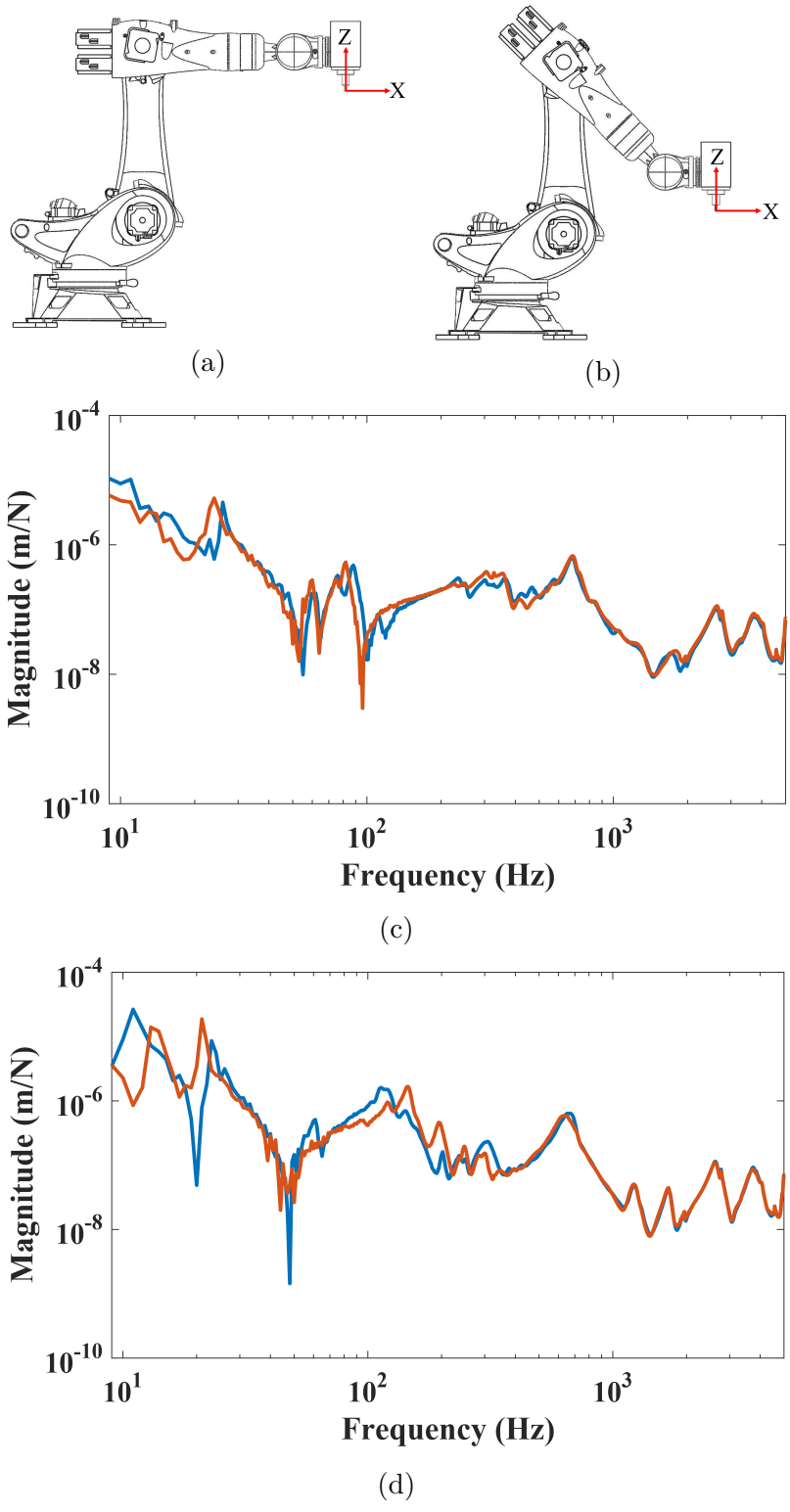

Figure 1.3: Configuration dependant FRF in an articulated robot. (a) Posture 1 (——) (b) Posture 2 (——) (c) G_{XX} (d) G_{YY}.

Since the dynamics of CNC machine remain unchanged within their workspace, chatter modeling can be carried out in one posture and used anywhere else. This is not the case in robotic milling, and a posture dependent model of the robot dynamics needs to be included in chatter analysis.

Alici and Shirinzadeh[5] used an enhanced joint stiffness model, which could be used to predict TCP dynamics in Cartesian space as a function of joint stiffness parameters and robot configuration. Klimchik et al.[44] developed a compliance compensation method based on a non-linear stiffness model to reduce the effect of manipulator configuration during the milling process. Also, there are a few works available on selecting the optimum robot configuration for maximizing material removal rate during robotic milling[93, 84, 51]. Abele et al.[2] presented a model for the robot structure along with the identification of its parameters by focusing on the analysis of the systems stiffness, and its behavior during the milling process. Also, Mejri et al.[56] measured the variation of the TCP dynamic response by changing posture of a machining articulated robot, and analyzed its influence on milling stability.

Although numerous researchers studied robotic machining and its stability in the recent years, there was no systematic approach found which is able to predict stability of robotic machining systems as a function of their posture. Works conducted on stability of robotic machining could be classified in two main categories; either studying a very small workspace, to minimize effects of posture dependency, or choose a relatively large workspace and measure TCP dynamic response in multiple positions. This work,aims to develop an organized step by step method by which TCP dynamic response for different configurations of a serial robot can be predicted; this could be used to predict robotic machining stability as a function of robot posture. Although the TCP dynamic response is calculated for a simple case study (3 DOF robot with rigid links and flexible joints), the methodology could be used on more sophisticated systems with higher DOFs or nonlinear joint behaviors.

1.4 Outline of the thesis

Chapter 2 is dedicated to discussing the presented robot dynamics model, and the experimental setups used in this work. Dynamic parameter identification by means of the base inertial parameters of the robot will be discussed in Chapter 3. In Chapter 4, the dynamic response of the robot in various postures will be calculated by using a Multi-Body Dynamics (MBD) model with flexible joints. Finally, the prediction of robotic milling stability will be discussed at the end of Chapter 4.

Chapter 2

Dynamics of Articulated Robots

2.1 Introduction

The MBD models used to describe the dynamics of the milling robot are introduced in this chapter. Two MBD models are used in this work: a rigid MBD model with rigid joints, and a rigid MBD model with flexible joint. The equations governing the motion of both models, along with the kinematic model of the milling robot, are presented here. Moreover, the experimental setups used for identification of the dynamic models' parameters are described in this chapter.

2.2 Multi Body Dynamics model

The Rigid Link Rigid Joint (RLRJ) model is discussed in Section 2.2.1; this model will be used in Chapter 3 for the base inertial parameters identification of a general N Degrees Of Freedom (DOF) robot. Afterwards, this model will be updated to the general case of the Rigid Link Flexible Joint (RLFJ) model in Section 2.2.2, which is used for modeling robot vibrations during milling process. Different forms of the RLFJ model will be used later in Chapters 3 and 4 to identify dynamic parameters of the robot, and to predict dynamic response of the robot structure, respectively.

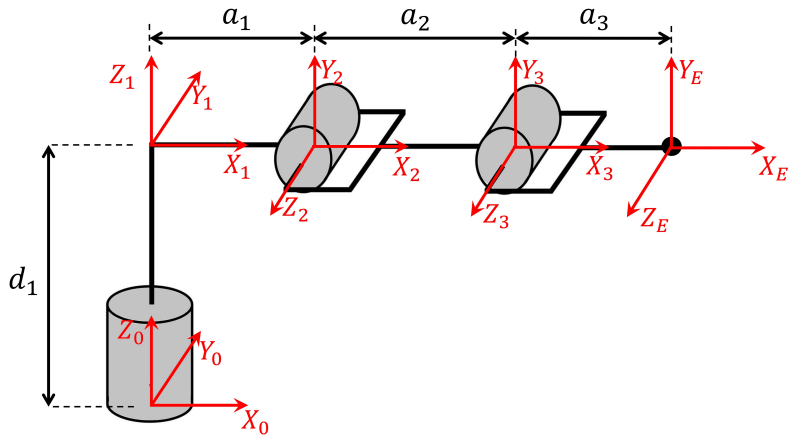

Figure 2.1: Simplified 3 DOF model and the definition of parameters in Table 2.1

2.2.1 Rigid Link and Rigid Joint

By adopting Craig's convention[20], and considering the first three degrees of freedom of an industrial robot, the kinematic model of an industrial robot with rigid links and rigid joints is described as shown in Figure 2.1. Denavit-Hartenberg [74] table of this model is presented in Table 2.1, and the definition of parameters used in this table could be found in Figure 2.1. Here, all the joints are assumed rotational, where joint i connects links $i-1$ and i. Joint i variable (θ_i) is the angle between x_{i-1} and x_i measured around z_i.

Table 2.1: DH table for the 3 DOF model shown in Figure 2.1

i	α_{i-1}	a_{i-1}	d_i	q_i
1	0	0	d_1	q_1
2	$\pi/2$	a_1	0	q_2
3	0	a_2	0	q_3
end-effector	0	a_3	0	0

The reason for only considering the first three joints of the robot is the fact that the most flexible vibration mode-shapes of the robot structure are known to be generated by the flexibility in the first three joints, also known as positioning degrees of freedom. This assumption also reduces the size of the system of equations and makes the derivations simpler. All the derivations in this work could be extended to any general N-DOF serial robot, if necessary.

The differential equation of motion for an N-DOF system with rigid links and rigid joints

is as

$$D(q)\ddot{q} + C(q,\dot{q})\dot{q} + F_v\dot{q} + F_s sgn(\dot{q}) + G(q) = \tau, \tag{2.1}$$

where $q \in \mathbb{R}^{N\times 1}$ is the joint variables vector and its first and second time derivatives are $\dot{q}$ and $\ddot{q}$, respectively. Also, $\tau \in \mathbb{R}^{N\times 1}$ is the input torque vector of the joints. $D(q) \in \mathbb{R}^{N\times N}$ is the joint-space inertia matrix of the robot, which is symmetric and positive definite. $C(q,\dot{q}) \in \mathbb{R}^{N\times N}$ is the Christoffel matrix, which presents the centrifugal and Coriolis terms. Also, $G(q) \in \mathbb{R}^{N\times 1}$ is the gravity potential vector. $F_v \in \mathbb{R}^{N\times N}$ and $F_s \in \mathbb{R}^{N\times N}$ are the diagonal matrices of viscous damping and Coulomb friction coefficients, respectively.

Commonly the following two assumptions are made to obtain a closed form formulation for D, C *and* G matrices:

1. The kinetic energy, K , is only a quadratic function of the vector $\dot{q}$ as:

$$K = \frac{1}{2}\dot{q}^T D(q)\dot{q}. \tag{2.2}$$

2. The potential energy, P, is not a function of $\dot{q}$ and $\ddot{q}$:

$$P = P(q). \tag{2.3}$$

Assumptions 2.2 and 2.3 are valid for the case of industrial robots; therefore the closed form formulation of the dynamic matrices could be derived using the Euler-Lagrange equation[74]. As a result, the inertia matrix, D, will be a function of the joint variables vector (q), the mass of the links (m_i), and their inertia tensor (I_i), where $i = 1, 2, ..., N$:

$$D(q) = [d_{kj}] = \sum_{i=1}^{N} [m_i J_{v_i}(q)^T J_{v_i}(q) + J_{\omega_i}(q)^T R_i(q) I_i R_i(q)^T J_{\omega_i}(q)], \tag{2.4}$$

where I_i is described in i_{th} link frame, located at its center of gravity, and $R_i \in \mathbb{R}^{3\times 3}$ presents the i_{th} link rotation matrix. Also, J_{v_i} and J_{ω_i} are the upper part and lower part of the i_{th} link Jacobian matrix described in reference frame, which are defined as a function of joint variables vector by Equation 2.5.

$$v_i = J_{v_i}(q)\dot{q}, \quad \text{and} \quad \omega_i = J_{\omega_i}(q)\dot{q}, \tag{2.5}$$

in which, v_i and ω_i are linear and rotational velocities of the center of gravity of link i

described in the reference frame.

Christoffel matrix and gravity vector components are also obtained as shown in Equation 2.6 and 2.7, respectively.

$$C(q,\dot{q}) = [c_{kj}] \quad ; \quad c_{kj} = \sum_{i=1}^{N} \frac{1}{2} \left\{ \frac{\partial d_{kj}}{\partial q_j} + \frac{\partial d_{ki}}{\partial q_j} - \frac{\partial d_{ij}}{\partial q_k} \right\} \dot{q}_i, \tag{2.6}$$

$$G(q) = [g_k] \quad ; \quad g_k = \frac{\partial P}{\partial q_k}. \tag{2.7}$$

In the next subsection, the RLRJ model will be modified by considering the flexibility of the rotational joints.

2.2.2 Rigid Link and Flexible joint

Figure 2.2 shows a single DOF rotational joint with flexibility around its rotation axis.

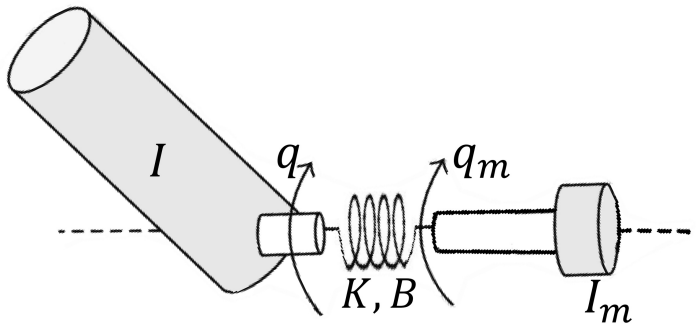

Figure 2.2: Model of a rotational joint with flexibility

The dynamics of N-DOF robots with the Single Degree Of Freedom (SDOF) flexible joint, shown in Figure 2.2, is described by[73]:

$$\begin{bmatrix} M(q) & 0 \\ 0 & M_m \end{bmatrix} \begin{Bmatrix} \ddot{q} \\ \ddot{q}_m \end{Bmatrix} + \begin{bmatrix} C(q,\dot{q}) + F_{v_q} + B & -B \\ -B & F_{v_{q_m}} + B \end{bmatrix} \begin{Bmatrix} \dot{q} \\ \dot{q}_m \end{Bmatrix}$$
$$+ \begin{bmatrix} F_{s_q} & 0 \\ 0 & F_{s_{qm}} \end{bmatrix} \begin{Bmatrix} sgn(\dot{q}) \\ sgn(\dot{q}_m) \end{Bmatrix} + \begin{bmatrix} K & -K \\ -K & K \end{bmatrix} \begin{Bmatrix} q \\ q_m \end{Bmatrix} + \begin{Bmatrix} G(q) \\ 0 \end{Bmatrix} = \begin{Bmatrix} \tau_{ext} \\ \tau \end{Bmatrix}, \tag{2.8}$$

where $q = [\ q_1 \ \cdots \ q_N\ ]^T$ is the instantaneous angular position of the links and $q_m = [\ q_{m_1} \ \cdots \ q_{m_N}\ ]^T$ is the corresponding rotor positions after gear reductions. The augmented link inertia (M) is a nonlinear function of the link positions vector (q) and contains the link inertia parameters as well as rotor inertia terms. M_m is the rotor inertia matrix, which is a diagonal matrix of the form $M_m(i,i) = r_i^2 I_{m_i}^{zz}$, where r_i is the gear ratio of i^{th} joint. By considering the typically high gear ratio of the industrial robot joints, coupling between the rotor and link inertia terms is neglected. The second term on the left hand side is the nonlinear damping matrix, which includes the Christoffel matrix $C(q,\dot{q})$, containing both the link and rotor inertia terms, the diagonal viscous friction coefficients matrix of the links (F_{v_q}) and rotors ($F_{v_{q_m}}$) motion, and the diagonal joint damping matrix B. The nonlinear damping matrix includes the diagonal Coulomb friction coefficients matrix of the links (F_{s_q}) and motors ($F_{s_{q_m}}$). The fourth term on the left hand side of Equation 2.8 shows the joint stiffness matrix(K). $G(q)$ is the gravity vector which is a function of robot position and contains link and rotor inertia parameters. The actuation torque applied on the rotors are denoted τ and the external torque reflected on the joints is τ_{ext}.

2.3 Experimental Setup

The two industrial robots used in this work as the experimental case studies are introduced in this Section. The case studies include the Staubli-TX200 robot located in University of Mons and the Kuka-KR90-R3100-HA robot at the University of Victoria.

2.3.1 Staubli TX200

This robot (See Figure 2.3) is a 6 axis industrial robot with a maximum payload of 130 Kg[91]. This specific robot is equipped with a spindle that gives the robot ability to perform milling operations.

Figure 2.3: Staubli TX200 robot

The kinematic chain when only considering the first three joints of this robot based on the model described in Figure 2.1 can be expressed by Table 2.2.

Table 2.2: DH table parameters for Staubli TX200

i	$\alpha_{i-1}(rad)$	$a_{i-1}(m)$	$d_i(m)$	$q_i(rad)$
1	0	0	0.642	q_1
2	$\pi/2$	0.25	0	q_2
3	0	0.95	0	q_3
end-effector	0	0.994	0	0

Staubli TX200 gravity compensation mechanism

Various gravity compensation mechanisms are used to reduce the gravitational load on the joints of industrial robots. Arakelian[9] presents an overview of gravity compensation methods applied in robotics. The gravity compensation mechanism in the Staubli TX200 robot includes a passive mechanism using linear springs. Figure 2.4 shows the schematic of this compensating mechanism.

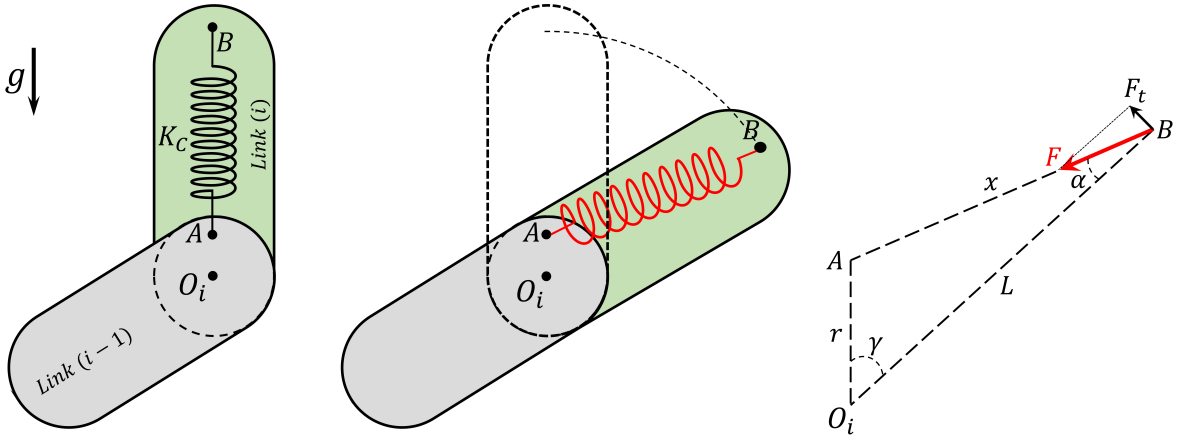

Figure 2.4: Schematic model of Staubli TX200 gravity compensation mechanism.

In Figure 2.4, point O_i is the i^{th} joint rotation axis, point A is fixed on link$(i-1)$ and point B is located on link(i). Also, O_iA which is fixed on link$(i-1)$ must be parallel to gravity vector direction $\hat{g}$. The minimum gravity compensation torque is applied when AB and O_iA are aligned. The compensation torque around O_i is obtained by using:

$$T_{O_i} = LK_C r\ sin(\gamma)\left(1 - \frac{x_0}{\sqrt{L^2 + r^2 - 2Lr\ cos(\gamma)}}\right). \tag{2.9}$$

The relationship between the geometric parameters used in Equation 2.9 are shown in Figure 2.4, while x_0 is the initial length of the spring.

The gravity compensation mechanism is implemented on second joint of Staubli TX200 robot. When this joint is at $\frac{\pi}{2}\ rad$ the compensation torque is negligible. As the joint angle deviates from $\frac{\pi}{2}\ rad$, the gravity compensation mechanism provides more torque. Compensation torque is maximized when this joint reaches $0\ rad$ or $\pi\ rad$. Therefore, the gravity compensator torque based on the position of the second joint can be obtained by inserting $\gamma = \frac{\pi}{2} - q_2$ in Equation 2.9:

$$\tau_{GC} = LK_C r\cos(q_2)\left(1 - \frac{x_0}{\sqrt{L^2 + r^2 - 2Lr\sin(q_2)}}\right). \tag{2.10}$$

Oueslati et al.[60] used a similar equation for gravity compensation torque of a Staubli RX-170B robot. Equation 2.9 is periodic in terms of q_2, therefore, following Swevers et al.[78], gravity compensation torque can be approximated using a finite number of cosine terms in

its Fourier series expansions. The first three terms are considered in this work:

$$\tau_{GC} = \sum_{n=1}^{3} B_n \cos(nq_2). \tag{2.11}$$

Note that τ_{GC} is implemented as an external torque in the second term of τ_{ext} in Equation 2.8.

2.3.2 Kuka KR90 R3100 HA

The Kuka robot (See Figure 2.5) located in the University of Victoria, is a 6 axis industrial robot with maximum payload equal to 90 Kg[88]. Although this robot is currently used for polishing operations, once a milling end-effector is installed, it can be used as a milling robot.

Figure 2.5: Kuka KR90 R3100 HA robot

The DH parameters of the Kuka robot that will be used in its kinematic model is shown in Table 2.3.

Table 2.3: DH table parameters for Kuka robot

i	$\alpha_{i-1}(rad)$	$a_{i-1}(m)$	$d_i(m)$	$q_i(rad)$
1	0	0	0.675	q_1
2	$\pi/2$	0.35	0	q_2
3	0	1.35	0	q_3
end-effector	0	1.615	0	0

Kuka KR90 gravity compensation mechanism

Unlike Staubli TX200, which employs a passive gravity compensator, Kuka robot is using an active pneumatic mechanism to compensate for the gravitational loads effecting on the second joint. Figure 2.6 presents the schematic view of this mechanism along with the view of this system on the robot. A detailed study about this type of gravity compensator is available in Klimchik et al.[45, 47, 46].

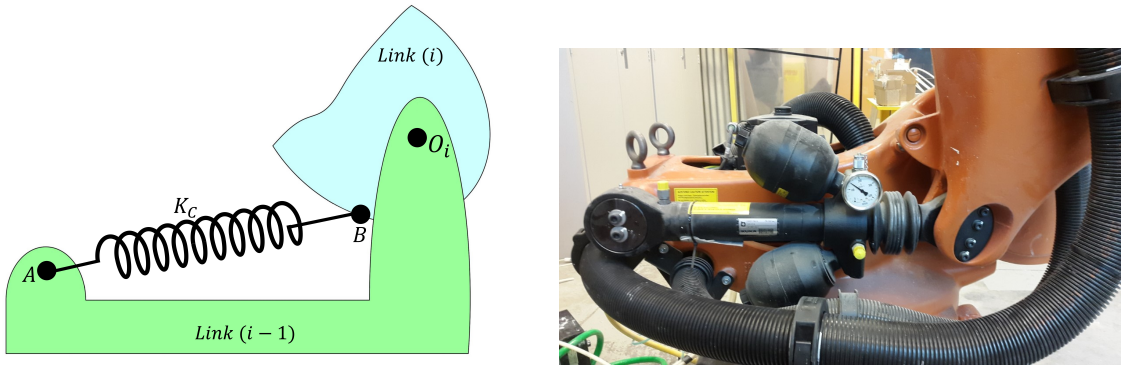

(a) (b)

Figure 2.6: (a) Schematic model of Kuka KR90 gravity compensation mechanism (b) View of Kuka KR90 gravity compensator.

Although the two gravity compensation mechanisms are looking different, they are both governed by a similar closed form formula (Equation 2.10). As a result, this system can be modeled by Equation 2.11 as well.

Chapter 3

Identification of Rigid Body Dynamics

3.1 Introduction

The experimental identification of the robot's rigid body dynamics model is essential for various applications such as advanced model-based control algorithms, numerical simulations of robot performance, and planning accurate trajectories[15]. Every standard robot identification procedure involves modeling, experiment design, data acquisition, signal processing, parameter estimation, and model verification[80]. Dynamic parameter identification of manipulators has attracted many researchers to work on this topic. Atkeson et al.[13] estimated inertial parameters of a manipulator by general movements. Grotjahn et al.[31] used a two step method to identify friction and inertial parameters of the manipulator using a rigid body model. Gautier et al.[27] proposed an identification method by using only the torque signal. Vast majority of the available dynamic identification methods could be categorized into two main categories: offline identification and online identification. In offline procedures, all the input-output signals are measured and recorded before processing while in online procedures parameters get identified and updated while the robot is operating. In this work, the offline identification procedures are studied. Offline identification methods could be divided into three main categories[86]:

1. **Physical experiments:** This method includes disassembling the robot structure to isolate each link of the robot, and using various methods to identify the inertial parameters of each link. For instance, Armstrong et al.[11] simply weighted links of the robot to measure their mass, determined position of center of mass of each link by determining counterbalanced points, and used two wire suspension experiments to identify elements of inertia tensor for each link. Da Lio et al.[21] developed a

mechanism by which they could identify inertial parameters of large mechanical systems through using a frequency domain approach. The physical experiments approach is not very popular among researchers since it requires considerable amount of effort, special measuring devices, and precise experimental setups.

2. **CAD methods:** Although this method is known to be the simplest method, it generally lacks desired accuracy since the CAD model provided by the manufacturer only contains the exterior shape of the links[41]. Also, this method is not able to predict damping parameters of the robot.

3. **System identification methods:** This method generally studies the "input-output" behavior of the system. It estimates the parameter values by minimizing the error between an experimental and simulated set of values when the system performs a specific task. Guegan et al.[32] used this method to predict 43 base parameters for a parallel kinematic system. This method is used by many scholars[67, 77, 29] and is known to be the most comprehensive and precise method between the three methods discussed in this section. As a result, this method is used in this manuscript to identify dynamic parameters of the robot.

In this chapter, first in Section 3.2 the theory of robot dynamic parameter identification is discussed; then, the experimental results are presented in Section 3.3.

3.2 Theory

Identification of robot inertial parameters is based on using the inverse dynamic model of the robot. The base parameters of the robot are the minimum number of parameters that are needed to express the rigid body dynamics of the robot [28]. The significance of the base parameter is due to the fact that the generally nonlinear equation of motion of the robot is linear in terms of its base parameters, which are combinations of the link inertial parameters. The size of base parameters vector depends on the DOFs of the robot and its kinematic chain [55].

When the joints' flexibility is neglected, i.e. $q_{m_i} = q_i$, Equation 2.8 is simplified into Equation 3.1 describing the dynamics of the RLRJ system:

$$D(q)\ddot{q} + C(q,\dot{q})\dot{q} + F_V\dot{q} + F_S\ sgn(\dot{q}) + G(q) = \tau + \tau_{ext}, \tag{3.1}$$

where $D(q) = M(q) + M_m$ is the combined link and rotor inertia matrix, $F_V = F_{v_q} + F_{v_{qm}}$ is the diagonal combined viscous damping coefficients matrix, and $F_S = F_{s_q} + F_{s_{qm}}$ is the diagonal combined Coulomb damping coefficients matrix. As mentioned, Equation 3.1 is linear in terms of the base parameters and it can be rewritten in the following linear form:

$$\Phi(q, \dot{q}, \ddot{q})\psi = \tau, \tag{3.2}$$

where ψ is the vector of base parameters. The derivation of the base parameters for a 3-DOF manipulator used in this work will be described in Section 3.2.1. Figure 3.1 shows the step by step overview of the dynamic parameter identification procedure for robots. The RLRJ model will be used to define and identify base parameters for the case of 3 DOF robot with considering rotor inertia parameters.

3.2.1 Base parameters formulation of the dynamic equation

Derivations in this section are performed based on Mayeda et al.[55], by adopting the augmented link model along with using Craig's convention. By using the RLRJ model from Equation 3.1 each robot DOF will have a total of 14 inertial parameters: m_i, m_{m_i} , $m_i r_i^x$, $m_i r_i^y$, $m_i r_i^z$, I_i^{xx}, I_i^{xy}, I_i^{xz}, I_i^{yy}, I_i^{yz}, I_i^{zz}, $I_{m_i}^{xx}$, $I_{m_i}^{yy}$, $I_{m_i}^{zz}$. Here m_i and m_{m_i} are the mass of link i and rotor i, respectively. ${}^i r_i$ is the center of gravity position for link i described in link i frame, and ${}^i I_i$ shows the inertia matrix of link i described in link i frame;

$${}^i r_i = \begin{bmatrix} r_i^x \\ r_i^y \\ r_i^z \end{bmatrix}, \qquad {}^i I_i = \begin{bmatrix} I_i^{xx} & -I_i^{xy} & -I_i^{xz} \\ -I_i^{xy} & I_i^{yy} & -I_i^{yz} \\ -I_i^{xz} & -I_i^{yz} & I_i^{zz} \end{bmatrix}, \qquad {}^i I_{m_i} = \begin{bmatrix} I_{m_i}^{xx} & 0 & 0 \\ 0 & I_{m_i}^{yy} & 0 \\ 0 & 0 & I_{m_i}^{zz} \end{bmatrix}. \tag{3.3}$$

By grouping the inertial parameters of the 3 DOF robot model described in Figure 2.1, based on the RLRJ model, 18 inertial parameters could be found. Formulation of the base parameters for the general N DOF robot is described in Appendix A. By having the base inertial parameters and adding the combined viscous and damping coefficient terms (F_V and F_S) along with the gravity compensation Fourier terms (B_i), a total of 27 identifiable dynamic parameters are found. The list of the 27 identifiable base dynamic parameters is available in Table 3.1.

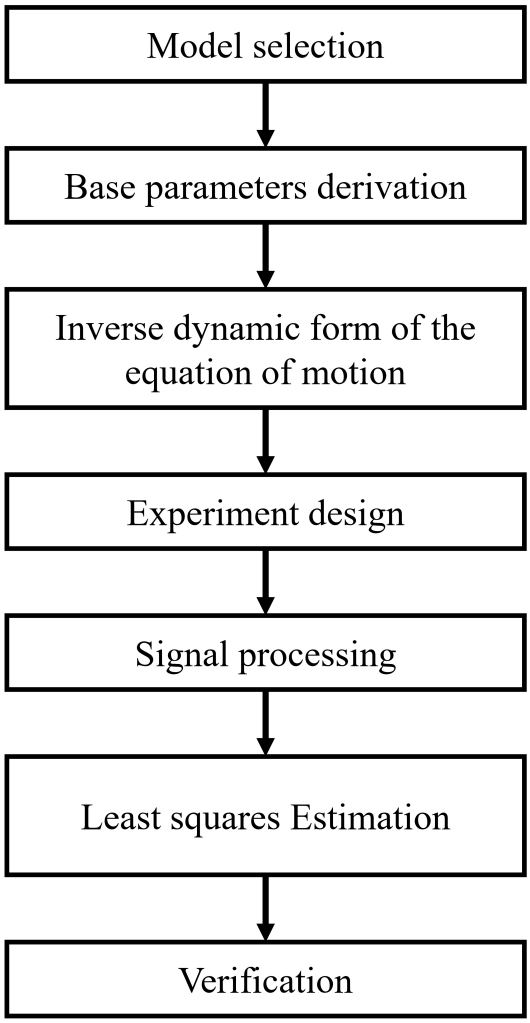

Figure 3.1: Course of action for dynamic identification of robots.

Table 3.1: List of dynamic parameters and their value for the Staubli TX200

Parameter number	Parameter description	Unit
1	$I_1^{zz} + I_{m_1}^{zz} r_1^2 + I_2^{yy} + I_{m_2}^{yy} + I_3^{yy} + I_{m_3}^{yy}$ $+ (m_2 + m_{m_2} + m_3 + m_{m_3}) (a_1)^2 + (m_3 + m_{m_3})(a_2)^2$	$Kg.m^2$
2	$I_2^{zz} + I_{m_2}^{zz} r_2^2 + (m_3 + m_{m_3})(a_2)^2$	$Kg.m^2$
3	$r_2^x m_2 + a_2(m_3 + m_{m_3})$	$Kg.m$
4	$r_2^y m_2$	$Kg.m$
5	$I_2^{xx} - I_2^{yy} - (m_3 + m_{m_3})(a_2)^2$	$Kg.m^2$
6	$I_2^{xz} + r_3^z a_2 m_3$	$Kg.m^2$
7	I_2^{xy}	$Kg.m^2$
8	I_2^{yz}	$Kg.m^2$
9	I_3^{zz}	$Kg.m^2$
10	$r_3^x m_3$	$Kg.m$
11	$r_3^y m_3$	$Kg.m$
12	$I_3^{xx} - I_3^{yy}$	$Kg.m$
13	I_3^{xz}	$Kg.m^2$
14	I_3^{xy}	$Kg.m^2$
15	I_3^{yz}	$Kg.m^2$
16	$I_{m_3}^{zz}$	$Kg.m^2$
17	$I_{m_2}^{xx} - I_{m_2}^{yy}$	$Kg.m^2$
18	$I_{m_3}^{xx} - I_{m_3}^{yy}$	$Kg.m^2$
19	B_1	$N.m$
20	B_2	$N.m$
21	B_3	$N.m$
22	F_{V_1}	$N.m.sec$
23	F_{S_1}	$N.m$
24	F_{V_2}	$N.m.sec$
25	F_{S_2}	$N.m$
26	F_{V_3}	$N.m.sec$
27	F_{S_3}	$N.m$

3.2.2 Inverse dynamics model

The goal in this section is to formulate the inverse dynamic model of the robot, which is linear in terms of the known base parameters (ψ). For a general N DOF system one can define $\Phi(q, \dot{q}, \ddot{q})$ as presented in

$$\Phi_{ij} = \frac{\partial \tau_i}{\partial \psi_j} \qquad \begin{cases} \forall i \in [1, N] \subset \mathbb{N} \\ \forall j \in [1, N_p] \subset \mathbb{N} \end{cases}, \tag{3.4}$$

where N_p is the number of base parameters of the robot. Note that in Equation 3.4, ψ_j could be a linear combination of inertial parameters while partial derivation is carried out by using a single variable. Consequently, the partial derivation is conducted by using the variable which is not available in any of the other base parameters.

By applying this method on the 3 DOF RLRJ model, $\Phi(q, \dot{q}, \ddot{q}) \in \mathbb{R}^{3\times 27}$ can be formulated. Definition of elements of Φ is available in Appendix B.

A similar procedure could also be used for each of the dynamic matrices of the system (D, C, and G), which results in expressing these matrices as a function of q (and $\dot{q}$ for the Christoffel matrix) and base parameters of the robot.

3.2.3 Least squares estimation

The method of least squares is aiming to minimize the mean of the quadratic norm of the prediction error ($\hat{e}$) for a set of data[52]. By having the inverse dynamic model of the system, a Multi-Input Multi-Output (MIMO) Least Square Estimation (LSE) can be used to identify dynamic parameters of the robot; where the inputs are the joints' position, velocity, and acceleration; The output is the corresponding joints' torque signal. By repeating Equation 3.2 at every sampling time-step $(t_1, ..., t_k)$ Equation 3.5 can be formulated.

$$A\psi = T + \hat{e} \tag{3.5}$$

where $A \in \mathbb{R}^{Nk\times N_p}$ is the regressor matrix, $\psi \in \mathbb{R}^{N_p\times 1}$ is the unknown dynamic parameters vector, $T \in \mathbb{R}^{Nk\times 1}$ is the torque vector, and $\hat{e}$ shows the output prediction error.

$$A = \begin{bmatrix} \Phi(q_{t_1}, \dot{q_{t_1}}, \ddot{q_{t_1}}) \\ \vdots \\ \Phi(q_{t_k}, \dot{q_{t_k}}, \ddot{q_{t_k}}) \end{bmatrix} \qquad T = \begin{bmatrix} \tau_{t_1} \\ \vdots \\ \tau_{t_k} \end{bmatrix}. \tag{3.6}$$

Formulating the experimental data in this format results in estimating the dynamic parameters of the robot from Equation 3.7. More information on this topic is available in[36, 12, 48, 52].

$$\psi = (A^T A)^{-1} A^T T, \tag{3.7}$$

Equation 3.7 has a solution under the assumption that $(A^T A)$ is positive definite, which means that the columns of matrix A must be linearly independent[48]. Since inverse dynamic model is derived by using the base parameters, columns of matrix A will be linearly independent.

3.2.4 Experiment design

The goal of experiment design is to adjust the experimental conditions so that maximal information is gained from the experiments[69]. Experiment design is an essential part of system identification procedure and can be found in system identification texts[52, 65]. To minimize the effect of noise on least squares solution in robot dynamic identification, a persistently exciting trajectory is required which equally excites all dynamic parameters of the robot[26]. Since condition number of the the regressor matrix ($cond(A)$) presents an upper limit for input/output error transmissibility[29], the selected input signals must form a well-conditioned regressor matrix (A). Different methods are available in the literature to design optimized exciting trajectories[10, 53, 64, 79].

In this work, the periodic excitation proposed by Swevers et al.[77] is used, which assumes the general form of excitation trajectory for each joint as a finite sum of sine and cosine functions as in a finite Fourier series;

$$\begin{aligned}
q_i(t) &= \sum_{h=1}^{N_h} \frac{a_h^i}{\omega_f h} \sin(\omega_f h t) - \frac{b_h^i}{\omega_f h} \cos(\omega_f h t) + q_{i_0}, \\
\dot{q}_i(t) &= \sum_{h=1}^{N_h} a_h^i \cos(\omega_f h t) + b_h^i \sin(\omega_f h t), \\
\ddot{q}_i(t) &= \sum_{h=1}^{N_h} -a_h^i \omega_f h \sin(\omega_f h t) + b_h^i \omega_f h \cos(\omega_f h t),
\end{aligned} \tag{3.8}$$

with a fundamental frequency of ω_f for all degrees of freedom. Using periodic trajectories, results in a periodic excitation at all joints with a period of $T_f = \frac{2\pi}{\omega_f}$. Consequently, for each

DOF of the robot $2N_h+1$ design parameters (δ_i) are needed based on the system constraints and optimized excitation trajectory. To find the design parameters, first, $\Phi(q, \dot{q}, \ddot{q})$ needs to be written as a function of the design parameters ($\Phi_D(\delta, \omega_f, nT_s)$) based on Equation 3.8 in which T_s is the sampling period and $\delta \in \mathbb{R}^{(N(2N_h+1))\times 1}$ is the vector of exciting trajectory design parameters. Next, by selecting a fundamental frequency, the constrained optimization problem described in Equation 3.9 will be solved where the constraints of this optimization problem are as stated in Equation 3.11

$$\hat{\delta} = \arg\min_{\delta} \ cond(A(\delta, \omega_f, T_s)), \tag{3.9}$$

here

$$A(\delta, \omega_f, T_s) = \begin{bmatrix} \Phi_D(\delta, \omega_f, T_s) \\ \vdots \\ \Phi_D(\delta, \omega_f, kT_s) \end{bmatrix} = \begin{bmatrix} \Phi(q_{t_1}, \dot{q_{t_1}}, \ddot{q_{t_1}}) \\ \vdots \\ \Phi(q_{t_k}, \dot{q_{t_k}}, \ddot{q_{t_k}}) \end{bmatrix}, \tag{3.10}$$

$$\begin{cases} q_{i_{min}} \leq q_i(\delta, nT_s) \leq q_{i_{max}} \\ \dot{q}_{i_{min}} \leq \dot{q}_i(\delta, nT_s) \leq \dot{q}_{i_{max}} \\ \ddot{q}_{i_{min}} \leq \ddot{q}_i(\delta, nT_s) \leq \ddot{q}_{i_{max}} \\ \{s\left(q(\delta, nT_s)\right)\} \subseteq \mathbb{S} \end{cases} \qquad \forall n \in [0, k] \subset \mathbb{W}. \tag{3.11}$$

In Equation 3.11, $q_{i_{min}}$, $q_{i_{max}}$, $\dot{q}_{i_{min}}$, $\dot{q}_{i_{max}}$, $\ddot{q}_{i_{min}}$,$\ddot{q}_{i_{max}}$ are the minimum and maximum possible values for joint position, joint velocity, and joint acceleration, respectively. Also, $s(q(\delta, nT_s))$ is the work-space used by the robot while moving on the trajectory, which needs to be a subset of the available work-space of the robot $\mathbb{S}$.

To solve this constrained optimization problem MATLAB software's "$fmincon$" function, which is a powerful tool for solving constrained nonlinear optimization problems, is used.

3.2.5 Signal processing

By moving the robot on the designed trajectory, the joints' positions and commanded torque signals are recorded. In order to employ the measured signals in the LSE, their high frequency noise must to be removed. Also, joint velocity and acceleration signals should be calculated by differentiating the joint position signals. Presence of high frequency noise in

the measured signals makes the differentiation error significantly large; this also emphasizes on the importance of signal processing in dynamic identification of robots.

To minimize the noise in the measured signals, a frequency domain low-pass filter is used which performs fast Fourier transform (FFT) filtering. $\dot{q}$ and $\ddot{q}$ signals are generated by differentiating the filtered joint position signal resulting from FFT low-pass filtering of the recorded joint position signals. Thus,by transferring the signal to frequency domain, performing differentiation in frequency domain once and twice (to generate $\dot{q}$ and $\ddot{q}$, respectively), and transferring the resulting signals back to the time domain, filtered joint velocity and acceleration signals are calculated. Figure 3.2 presents the schematic of the signal processing procedure used in this work.

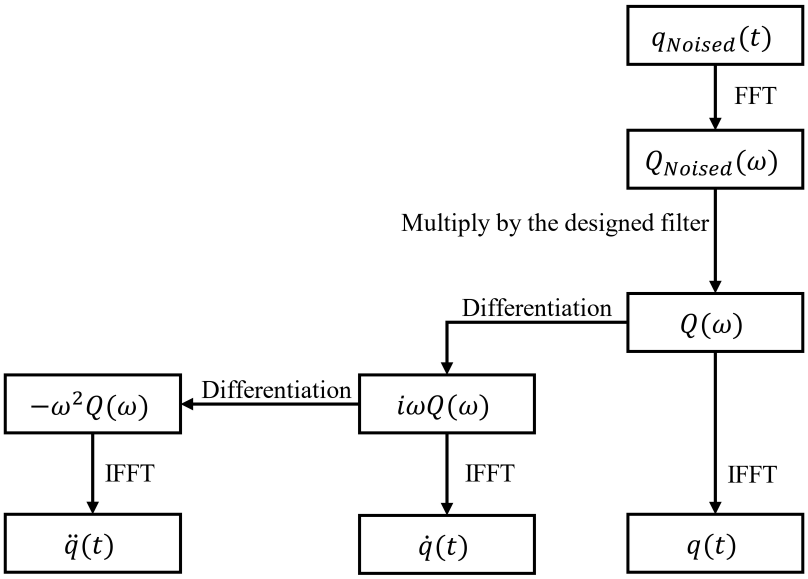

Figure 3.2: An overview of the frequency domain filtering and differentiation.

3.3 Experimental Validation

In order to verify the dynamic parameter identification procedure, two experimental setups are used which are briefly introduced in Section 2.3. First, the identification procedure on the Staubli TX200 robot will be discussed and then the same procedure will be implemented on the Kuka KR90 R3100 robot.

3.3.1 Staubli robot

A brief introduction on the Staubli TX200 robot can be found in Section 2.3.1. In order to generate a persistently exciting trajectory as described in Section 3.2.4, the constraining parameters of the system both in joint-space and Cartesian space are required based onn Equation 3.11. Table 3.2 defines the motion-constraining parameters for the Staubli TX200 robot.

Table 3.2: Motion constraining parameters for Staubli TX200

Type of constraint	Variable	Value
Joint-space reach (rad)	$q_{1_{max}}$	0.5236
	$q_{1_{min}}$	-2.531
	$q_{2_{max}}$	2.618
	$q_{2_{min}}$	-0.4892
	$q_{3_{max}}$	0.14
	$q_{3_{min}}$	-2.269
Joint speed$(\frac{rad}{s})$	$\dot{q}_{1_{max}}$	2.618
	$\dot{q}_{2_{max}}$	2.618
	$\dot{q}_{3_{max}}$	2.618
Joint acceleration$(\frac{rad}{s^2})$	$\ddot{q}_{1_{max}}$	$NA^{\star}$
	$\ddot{q}_{2_{max}}$	NA
	$\ddot{q}_{3_{max}}$	NA
Cartesian space reach (m)	X_{max}	2
	X_{min}	-1
	Y_{max}	1
	Y_{min}	-2
	Z_{max}	2.586
	Z_{min}	0.5

* Not available

In Table 3.2, joint-space reach and joint speed values are obtained from the user manual supplied by the manufacturer. Since there is no maximum joint acceleration defined in this manual, no constraint was applied on joint accelerations. The X, Y, and Z axis in Cartesian space reach are defined based on X_0, Y_0, and Z_0 in Figure 2.1, where the origin is positioned on the ground. The Staubli robot is mounted on a steel slab with an approximate height of

Z_{min} from the ground.

Using the information available in Table 2.2 and Table 3.2 the constrained optimization problem from Equation 3.9 can be solved by using different initial values to find a few persistently exciting trajectories. By selecting $\omega_f = 0.1\ Hz$ and $N_h = 5$, six optimally exciting trajectories were obtained and the robot was programmed to follow them in the automatic mode.

The robot repeatedly moves on each trajectory while the joint positions and the commanded joint torque signals are recorded. Afterward, by conditioning, differentiating, and removing the transitional recorded signals, the identification of dynamic parameters is performed.

By employing LSE, dynamic parameters by which the model accurately predicts the commanded torque signals are estimated. Table 3.3 shows the identified dynamic parameters of the Staubli TX200 robot.

Table 3.3: Identified dynamic parameters of Staubli TX200

Parameter number	Parameter description	Value
1	$I_1^{zz} + I_{m_1}^{zz} r_1^2 + I_2^{yy} + I_{m_2}^{yy} + I_3^{yy} + I_{m_3}^{yy}$ $+ (m_2 + m_{m_2} + m_3 + m_{m_3}) (a_1)^2 + (m_3 + m_{m_3})(a_2)^2$	919.09
2	$I_2^{zz} + I_{m_2}^{zz} r_2^2 + (m_3 + m_{m_3})(a_2)^2$	708.51
3	$r_2^x m_2 + a_2(m_3 + m_{m_3})$	253.51
4	$r_2^y m_2$	-9.75
5	$I_2^{xx} - I_2^{yy} - (m_3 + m_{m_3})(a_2)^2$	-315.85
6	$I_2^{xz} + r_3^z a_2 m_3$	-41.34
7	I_2^{xy}	-38.95
8	I_2^{yz}	-3.20
9	I_3^{zz}	132.10
10	$r_3^x m_3$	123.26
11	$r_3^y m_3$	2.75
12	$I_3^{xx} - I_3^{yy}$	-143.21
13	I_3^{xz}	-8.89
14	I_3^{xy}	-8.80
15	I_3^{yz}	1.13
16	$I_{m_3}^{zz}$	0.0094
17	$I_{m_2}^{xx} - I_{m_2}^{yy}$	-0.0079
18	$I_{m_3}^{xx} - I_{m_3}^{yy}$	-0.0027
19	B_1	2562.6
20	B_2	-85.45
21	B_3	278.32
22	F_{V_1}	780.82
23	F_{S_1}	32.96
24	F_{V_2}	900.02
25	F_{S_2}	3.42
26	F_{V_3}	483.57
27	F_{S_3}	134.1

Identified dynamic parameters can be verified by comparing the measured and predicted torque signals for an arbitrary trajectory. As shown in Figure 3.3, the identified model

accurately estimates the joint torque signals for arbitrary trajectories. Table 3.4 shows the Root Mean Square (RMS) of the torque prediction percentage error for the arbitrary trajectory shown in Figure 3.3. The torque comparison and the RMS of the torque prediction percentage error for the trajectories used to identify the dynamic parameters can be found in Appendix C.

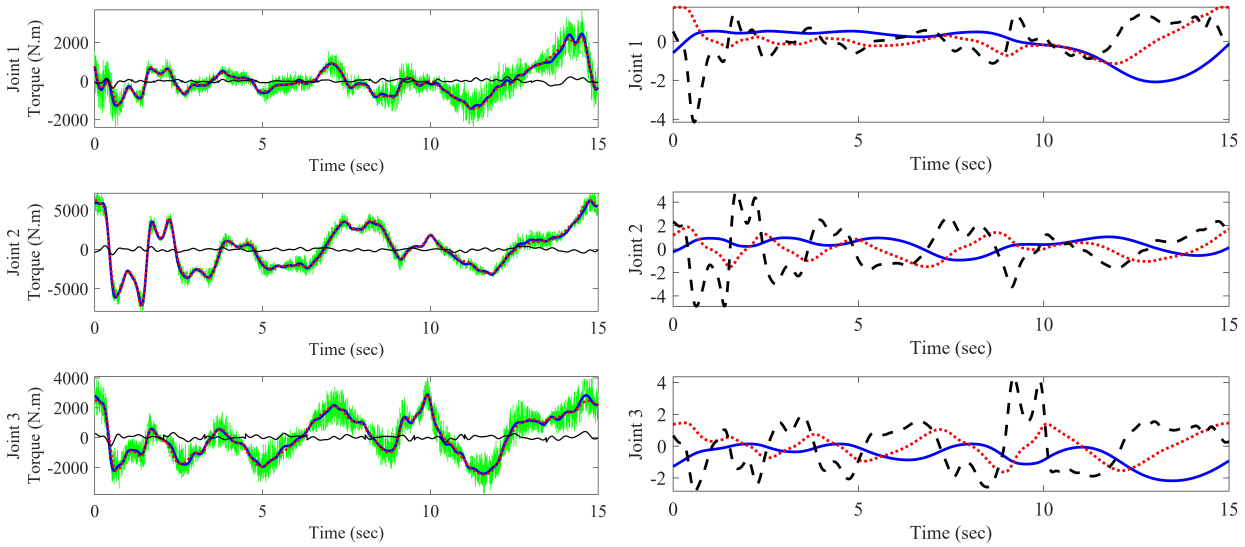

(a) (b)

Figure 3.3: (a) Measured and predicted torque for Staubli TX200 (Measured torque (——), Filtered torque (——), Predicted torque (- - -), Prediction error (——)).
(b) Joint-space position $[rad]$ (——), Joint-space velocity $[rad/sec]$ (- - -), and Joint-space acceleration $[rad/sec^2]$ (— —) for Staubli TX200.

Table 3.4: RMS of torque prediction percentage error in Figure 3.3

	Joint 1	Joint 2	Joint 3
RMS of $(\frac{T_{Measured}-T_{Predicted}}{T_{Measured}} \times 100)$	0.9%	0.5%	0.4%

3.3.2 Kuka robot

A similar approach is used for the Kuka KR90 R3100 robot. This system is introduced briefly in Section 2.3.2. The motion constraints for this robot are available in Table 3.5, where the definition of parameters used in this table are the same as Table 3.2.

Table 3.5: Motion constraining parameters for Kuka KR90

Type of constraint	Variable	Value
Joint-space reach (rad)	$q_{1_{max}}$	3.23
	$q_{1_{min}}$	-3.23
	$q_{2_{max}}$	2.44
	$q_{2_{min}}$	0.08
	$q_{3_{max}}$	2.1
	$q_{3_{min}}$	-2.7
Joint speed$(\frac{rad}{s})$	$\dot{q}_{1_{max}}$	1.83
	$\dot{q}_{2_{max}}$	1.76
	$\dot{q}_{3_{max}}$	1.87
Joint acceleration$(\frac{rad}{s^2})$	$\ddot{q}_{1_{max}}$	NA
	$\ddot{q}_{2_{max}}$	NA
	$\ddot{q}_{3_{max}}$	NA
Cartesian space reach (m)	X_{max}	2.6
	X_{min}	-1.5
	Y_{max}	1.4
	Y_{min}	-1.6
	Z_{max}	2.5
	Z_{min}	0.5

Kuka KR90 results

Similar to the identification process for the Staubli TX200, by employing LSE, the model parameters of Kuka KR90 robot are estimated and shown in Table 3.6.

Table 3.6: List of dynamic parameters and their values for the Kuka KR90

Parameter number	Parameter description	Value
1	$I_1^{zz} + I_{m_1}^{zz} r_1^2 + I_2^{yy} + I_{m_2}^{yy} + I_3^{yy} + I_{m_3}^{yy}$ $+ (m_2 + m_{m_2} + m_3 + m_{m_3}) (a_1)^2 + (m_3 + m_{m_3})(a_2)^2$	1892.88
2	$I_2^{zz} + I_{m_2}^{zz} r_2^2 + (m_3 + m_{m_3})(a_2)^2$	1463.98
3	$r_2^x m_2 + a_2(m_3 + m_{m_3})$	653.48
4	$r_2^y m_2$	51.49
5	$I_2^{xx} - I_2^{yy} - (m_3 + m_{m_3})(a_2)^2$	-652.62
6	$I_2^{xz} + r_3^z a_2 m_3$	33.36
7	I_2^{xy}	80.92
8	I_2^{yz}	-0.58
9	I_3^{zz}	163.97
10	$r_3^x m_3$	130.47
11	$r_3^y m_3$	-2.78
12	$I_3^{xx} - I_3^{yy}$	-157.71
13	I_3^{xz}	1.09
14	I_3^{xy}	3.04
15	I_3^{yz}	-0.95
16	$I_{m_3}^{zz}$	0.0112
17	$I_{m_2}^{xx} - I_{m_2}^{yy}$	0.0146
18	$I_{m_3}^{xx} - I_{m_3}^{yy}$	0.0115
19	B_1	-7736.22
20	B_2	-80.29
21	B_3	200.14
22	F_{V_1}	1365.67
23	F_{S_1}	319.08
24	F_{V_2}	1311.13
25	F_{S_2}	402.00
26	F_{V_3}	925.29
27	F_{S_3}	234.91

Identified dynamic parameters are verified by comparing measured and predicted torque signals for an arbitrary trajectory. Figure 3.4 shows the comparison of the commanded

and predicted torque signals for each joint of this robot when the robot is commanded to move on an arbitrary trajectory. Table 3.7 shows the RMS of the torque prediction error in Figure 3.4. The torque comparison and the RMS of the torque prediction percentage error for the trajectories used to identify Kuka KR90 dynamic parameters can be found in Appendix C.

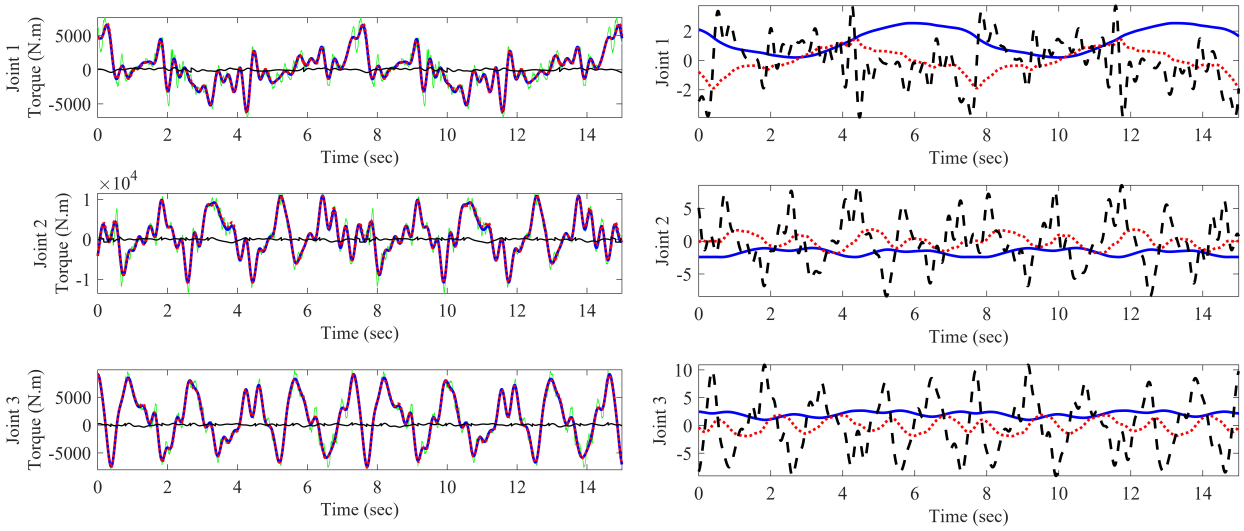

(a) (b)

Figure 3.4: (a) Measured and predicted torque for Kuka KR90 (Measured torque (——), Filtered torque (——), Predicted torque (- - -), Prediction error (——)).
(b) Joint-space position $[rad]$ (——), Joint-space velocity $[rad/sec]$ (- - -), and Joint-space acceleration $[rad/sec^2]$ (— —) for Kuka KR90.

Table 3.7: RMS of torque prediction percentage error for Kuka KR90

	Joint 1	Joint 2	Joint 3
RMS of $(\frac{T_{Measured}-T_{Predicted}}{T_{Measured}} \times 100)$	0.6%	0.6%	0.2%

Chapter 4

Dynamic Response Prediction and Milling Stability

4.1 Introduction

This chapter aims to predict the dynamic behavior of robots as a function of their posture. Knowing robots' dynamic behavior as a function of their posture can be used to predict the TCP Frequency Response Function (FRF) in Cartesian space. The TCP FRF is used to predict milling stability of robotic machining systems. To predict the posture-dependent dynamics of robot structure, a flexible joint model needs to be added to the RLRJ model used in Chapter 3. Dynamic modeling of manipulator joints is an important topic in the field of control. Although most works in this area were initially aiming toward rigid robot control, experimental data[76] demonstrated that the joint flexibility should not be neglected in modeling and control of manipulators, specially when high performance is required. Spong[73] proposed an elastic joint model to control manipulators with flexible rotary joints. This initiated more work on controlling flexible joint manipulators conducted by numerous researchers[30, 1, 42]. This model is also used by other authors to identify dynamic parameters of manipulator joints.

The model proposed by Spong[73], which is vastly used by researchers[18, 4], considers flexibility around rotation axis of the joint. Olabi et al.[59] used this method to identify each joint's stiffness separately by employing dead weights. Also, Dumas et al.[24] applied wrenches on the end-effector and measured the resulting displacement in Cartesian-space. Alici et al.[5] presented an enhanced stiffness modeling and a methodology for manipulator stiffness identification and characterization. Some authors consider two additional virtual

joints at each degree of freedom to consider flexibility perpendicular to the axis of joint motion[3, 63, 43]. In more complex cases, some consider the nonlinear stiffness models or the hysteresis and backlash effects on the joint dynamic behavior[18, 70, 72, 40].

Although the joint dynamic behavior is assumed to remain constant throughout its workspace, the resulting stiffness and damping matrices in taskspace are strongly posture dependent. Salisbury[71] was first to derive the conventional formula for mapping stiffness matrix between Cartesian and joint spaces. Choi et al.[17] present a generalized stiffness model between the joint-space and task-space stiffness.

Baglioni et al.[14] used a multibody modelling approach to predict the dynamic behavior of a machining robot. Bisu et al.[16] analyzed the dynamic behaviour of a machining robot in three phases of the robot application; first, while the robot is stationary and spindle is not working, second, while the spindle is turned on without cutting, and finally, while the cutting is in progress. Leonesio et al.[49] studied the pose-dependant dynamics in robotic milling experimentally. Villagrossi[83] studied modeling and control of robots for machining applications. Reinl et al.[68] adopted an offline concept to analyze, predict, and compensate for the deflections due to cutting forces in milling.

In this chapter, first, the dynamic model and the corresponding assumptions are reviewed (Section 4.2). Then, in Section 4.3, two methods will be introduced by which dynamic response of manipulators are calculated. Afterward, the joint parameter identification is discussed (Section 4.4). Next, in Sections 4.5 to 4.7, the conducted Experimental Modal Analysis (EMA) tests are discussed, the identified joint parameters are introduced and the results are verified. Finally, the milling stability of the robotic milling process is studied in Section 4.8.

4.2 Linearized Dynamics

Considering the low feed rate during robotic milling operations, the motion of the robot can be regarded as quasi-static, where the joint angles (q) only vary incrementally around the operating posture, q_0:

$$q = q_0 + \Delta q. \tag{4.1}$$

This results in the joints' velocity and acceleration to vary incrementally around zero:

$$\dot{q} = \Delta\dot{q} \quad \text{and} \quad \ddot{q} = \Delta\ddot{q}. \tag{4.2}$$

In addition, by assuming perfect performance of the joint controllers in regularizing the rotor position, the rotor rotation angles are assumed to remain constant at $G_R q_0$, where G_R is the diagonal matrix of joint gear ratios (r_i). By assuming negligible Coulomb damping forces, Equation 2.8 is written as:

$$M(q_0 + \Delta q)\Delta\ddot{q} + (C(q_0 + \Delta q, \Delta\dot{q}) + F_v + B)\Delta\dot{q} + K\Delta q + G(q_0 + \Delta q) = \tau_{ext}, \tag{4.3}$$

where τ_{ext} is the external exciting torque applied on the robot. The assumption of perfect performance of the joint controller is verified by Hearne[34] through doing two sets of impact testing on a robot, one while motor brakes were engaged and the other one while the motor brakes were released and robot controller was operating. The resulted response was the same for both cases. Equation 4.3 is linearized around q_0 resulting in Equation 4.4 for the free oscillation of this system.

$$M_0\Delta\ddot{q} + C_0\Delta\dot{q} + K_0\Delta q = 0, \tag{4.4}$$

in which based on the definition of the inertia, damping and stiffness matrix for Equation 4.3:

$$\begin{aligned} M_0 &= \left.\frac{\partial\tau_{ext}}{\partial\Delta\ddot{q}}\right|_{q_0} = M(q_0), \\ C_0 &= \left.\frac{\partial\tau_{ext}}{\partial\Delta\dot{q}}\right|_{q_0} = F_v + B, \\ K_0 &= \left.\frac{\partial\tau_{ext}}{\partial\Delta q}\right|_{q_0} = K + \left.\frac{\partial G(q_0 + \Delta q)}{\partial\Delta q}\right|_{q_0}. \end{aligned} \tag{4.5}$$

Here, $M(q_0)$ can be calculated by using the regressor (Φ) and identified base parameters (ψ) from Chapter 3, along with the rotor inertia matrix (M_m);

$$M(q_0) = \left(\left.\frac{\partial\Phi\psi}{\partial\ddot{q}}\right|_{q_0}\right) - M_m. \tag{4.6}$$

4.3 FRF Prediction Methods

This section will discuss different methods to predict FRF at the TCP in Cartesian space based on the RLFJ model in Equation 4.4. Three FRF prediction methods are introduced here:

1. **Finite Element Method (FEM):** This method is widely used in the structural dynamic applications because of its capability of handling complex geometries and coupled systems. This method can give very precise results if the joint dynamic behavior is known and a realistic CAD model of the robot is available. As a result, this method would be the ideal case when links flexibility is studied. FEM requires significantly higher computational cost compared to the two other methods introduced in this chapter, hence, this method will not be studied in this work.

2. **Multibody Dynamics Method:** The MBD method defines how a mechanical system, consisting of interconnected bodies through degrees of freedom, moves under the influence of applied forces. Although various commercial MBD software packages exist, an open source C++ library is used in this work.

3. **Inverse Dynamics analysis of FRF:** In this method, the TCP FRFs are computed from the joint space FRFs by employing the inverse kinematics and dynamics of the robot. MATLAB is used to conduct the programming for this method.

4.3.1 Multibody Dynamics Method

In this section, a MBD approach for calculating frequency response of the robotic systems based on the RLFJ model will be presented. EasyDyn is a C++ library for simulation of multibody dynamic systems or systems with first or second-order differential equations. This library is used to implement the MBD model of the robot. Figure 4.1 shows the procedure of generating TCP point FRF in Cartesian space using EasyDyn.

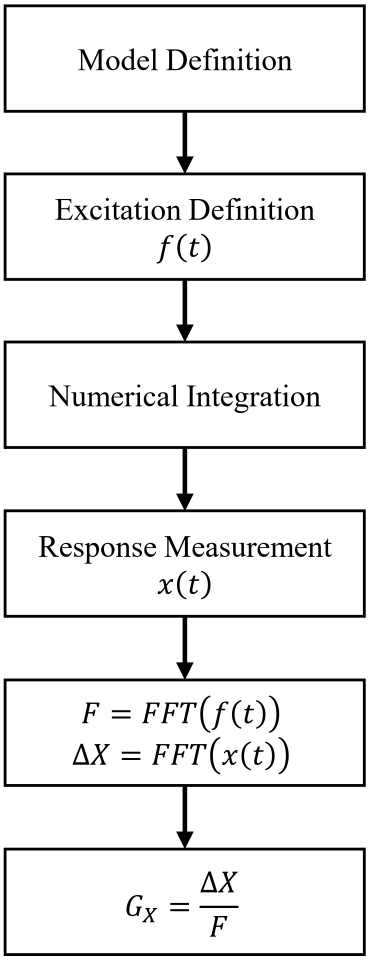

Figure 4.1: MBD procedure for calculating TCP frequency response in Cartesian space

The Model definition step consists of:

- Defining each body with its inertial parameters.
- Defining the degrees of freedom which results in definition of the kinematic chain of the system.
- Defining the joint dynamic behavior including joint damping and compliance.

Also, the model could be defined by using the base parameters of the robot described in Chapter 3. Afterward, by defining the excitation force as a chirp signal, the numerical integration will be carried out to obtain the system response to the applied force in time

domain. By transferring the input excitation and output displacement signals to frequency domain, one can have the FRF of the system as described in the last step of Figure 4.1.

Although the MBD method is much faster than FEM, the computational costs for this method are still high since a time domain numerical integration is used. A frequency domain method is introduced in the next subsection, which can predict the robot Cartesian space FRFs with a considerably lower computational cost.

4.3.2 Inverse Dynamics analysis of FRF

Since the joint stiffness and damping parameters (K and C_0 from Equation 4.4) are assumed constant throughout the joint-space, and due to the complex geometrical coupling between joint-space and taskspace, it is simpler to model the robot in joint-space. Considering the equation of motion in joint space, as described in Equation 4.4, joint-space FRF ($G_\theta(\omega) \in \mathbb{C}^{N\times N}$) is expressed by Equation 4.7,

$$G_\theta(\omega, q_0) = \frac{\Delta q}{\tau_{ext}} = \left(K_0 - \omega^2 M_0 + i\omega C_0\right)^{-1}. \tag{4.7}$$

For robotic machining applications, the TCP FRF in Carteisan space is required. Figure 4.2 shows the simplified procedure to calculate the TCP Cartesian space FRF based on the joint-space FRFs for any N DOF system. Here, F_e is the excitation force applied at the TCP, $J \in \mathbb{R}^{3\times N}$ is the TCP upper jacobian matrix which maps the excitation force applied at TCP to the joint-space torques (τ_e).

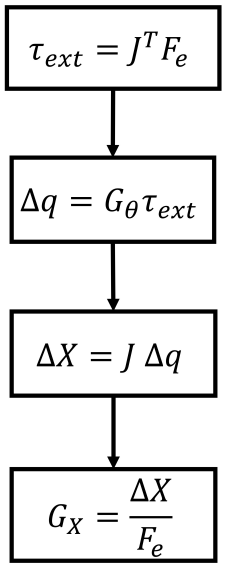

Figure 4.2: Simplified procedure for calculating Cartesian space FRF based on joint-space FRFs

Since Δq is the incremental joint displacement vector, FRF in Cartesian space (G_X) could be written in the form of Equation 4.8 by having the excitation applied at point i and the response measured at point j, [2]:

$$G_{X_{ij}}(\omega, q) = {}^{j}J_{v\ j}(q)\ G_\theta(\omega, q)\ {}^{i}J_{v\ i}^{\ T}(q). \tag{4.8}$$

Here, $G_X \in \mathbb{C}^{3\times3}$, and ${}^{i}J_{v\ i} \in \mathbb{R}^{3\times N}$ is the upper Jacobian matrix for point i formulated with respect to the local frame of point i as described in Equation 4.9.

$${}^{i}v_i = {}^{i}J_{v\ i}\ \dot{q}, \tag{4.9}$$

where ${}^{i}v_i$ is the velocity of point i described in the local frame of point i.

The most general case of FRFs in Cartesian space could be calculated by using the full $6 \times N$ Jacobian matrix which will result in $G_X \in \mathbb{C}^{6\times6}$; this general case is out of the scope of this work and will not be discussed further.

By using this method, TCP frequency response in Cartesian space is calculated with an extremely lower computational cost than the other methods introduced in this section. This makes the model identification based on the iterative model updating techniques easier and faster.

4.4 Joint Parameter Identification

By introducing the state vector $q_s = \begin{bmatrix}\Delta q^T & \Delta \dot{q}^T\end{bmatrix}^T$, Equation 4.4 can be expressed in its first order form as

$$\hat{\mathbf{A}}\dot{\mathbf{q}}_s + \hat{\mathbf{B}}\mathbf{q}_s = \mathbf{0}, \tag{4.10}$$

where $\hat{\mathbf{A}}$ and $\hat{\mathbf{B}}$ are system matrices:

$$\hat{A} = \begin{bmatrix} C_0 & M_0 \\ M_0 & 0 \end{bmatrix}, \ \hat{B} = \begin{bmatrix} K_0 & 0 \\ \mathbf{0} & -M_0. \end{bmatrix} \tag{4.11}$$

The natural frequencies of the robot structure are obtained from the generalized eigenvalues of $\hat{A}$ and $\hat{B}$ matrices [54]:

$$f_r = \frac{\sqrt{\lambda_r {\lambda_r}^*}}{2\pi}, \quad \text{and} \quad \zeta_r = -\frac{\mathrm{Re}(\lambda_r)}{\sqrt{\left(\mathrm{Re}(\lambda_r)\right)^2 + (2\pi f_r)^2}}, \tag{4.12}$$

where f_r and ζ_r, $(r = 1, 2, ..., N)$ are the natural frequencies and the corresponding modal damping ratios, respectively. The asterisk stands for the complex conjugate, and λ_r are the generalized eigenvalues:

$$Av_r\lambda_r = Bv_r. \tag{4.13}$$

The vectors, v_r, are the corresponding eigenvectors. Since $\hat{\mathbf{A}}$ and $\hat{\mathbf{B}}$ matrices are real, their generalized eigenvalues and eigenvectors appear in complex conjugate pairs. As a result, for the n-DOF arm, n pairs of eigenvectors and eigenvalues are obtained. Each pair of eigenvalues $(\lambda_r, {\lambda_r}^*)$ corresponds to one modal frequency (f_r), and each pair of eigenvectors (v_r, v_r^*) corresponds to the associated mode shape. Although the obtained mode shapes are in joint space, obtaining the mode shape in Cartesian space is straightforward using forward kinematics.

In this chapter, the stiffness and damping parameters of the joints are determined by using the modal parameters obtained in Section 4.5. Matching the modal parameters of the model and the experimental setup are carried out by manual adjustment of the unknown joint parameters (K and C_0 elements). Since a Single Degree Of Freedom (SDOF) joint model is used, only N modes can be identified with this method.

The Modal Assurance Criteria (MAC) is used to verify the correlation between two sets of modal vectors in this work. The MAC value between two modes is essentially the normalized

dot product of the complex modal vector at each common node as

$$MAC(v_r, v_s) = \frac{\left| v_r^{*T} v_s \right|^2}{\left(v_r^{*T} v_r \right) \left(v_s^{*T} v_s \right)}. \tag{4.14}$$

4.5 Experimental Modal Analysis

4.5.1 Staubli TX200

Modal properties of the Staubli TX200 robot were identified by conducting a set of (EMA) tests by Huynh et al.[37]. Figure 4.3 shows the selected excitation nodes for this setup.

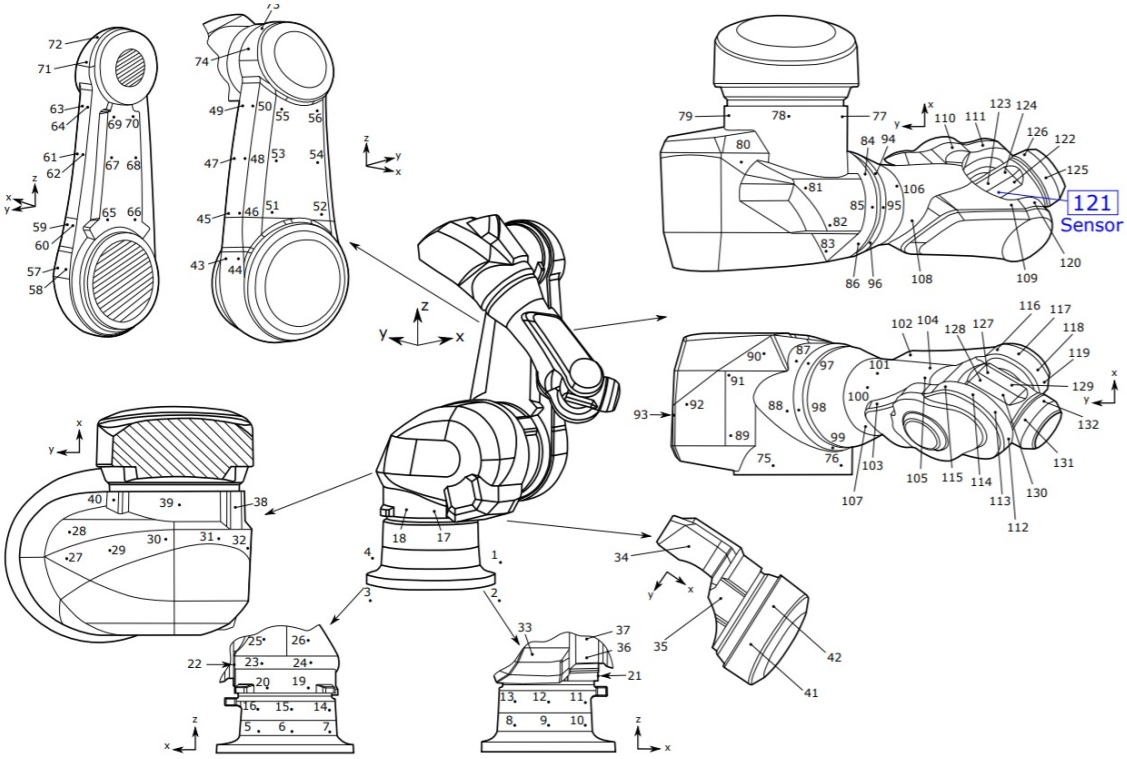

Figure 4.3: Selected nodes for the 3D EMA tests on Staubli TX200.[37]

A three axis "Dytran 3093B1" accelerometer, with a sensitivity of 100 mV/g, was fixed on node 121. Figure 4.4 shows the orientation of accelerometer axes. An impact hammer equipped with a "Dytran 1061V2" force sensor with a sensitivity of 890.47 N/V is used to excite the structure. A soft rubber tip is utilized to excite structural modes with lower frequencies.

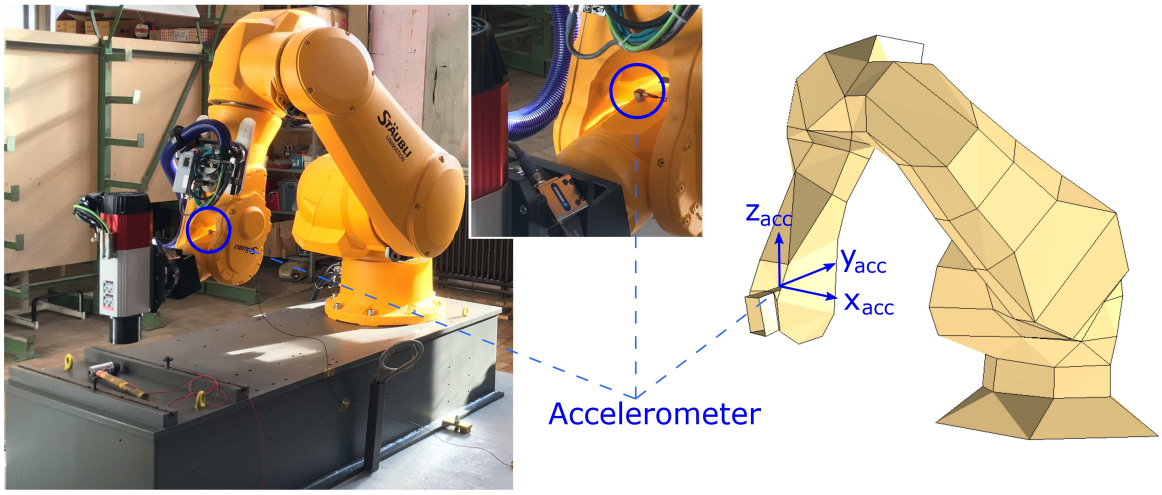

Figure 4.4: Sensor mounting position and orientation of accelerometer axes for Staubli TX200.[37]

Table 4.1 shows the configurations used to do the EMA testing on the Staubli TX200 robot. Since the EMA tests had been previously conducted by Huynh et al.[37], and were not designed by the author, fifth joint values are not fixed at zero. As a result, the inertia matrix cannot be exactly expressed by the 3 DOF identified model of Staubli TX200 robot in Chapter 3. To minimize the error caused by rotation of the fifth axis on the predicted inertia matrix, configurations with the smallest q_5 value are studied in this work.

Table 4.1: EMA testing configurations for Staubli TX200.

	Configuration 1	Configuration 2	Configuration 3
q_1	$-91°$	$-91°$	$-91°$
q_2	$57°$	$27°$	$33°$
q_3	$-84°$	$-43°$	$-71°$
q_4	$0°$	$0°$	$0°$
q_5	$12°$	$7°$	$22°$
q_6	$0°$	$0°$	$0°$
	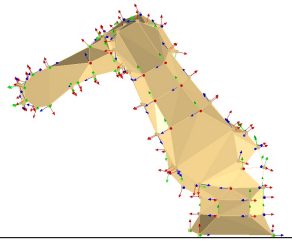	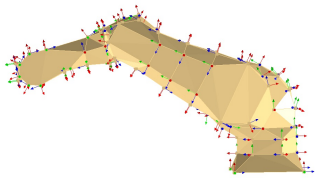	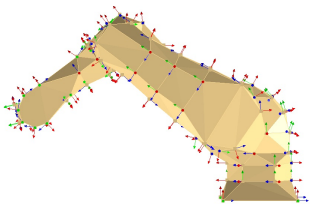

Modal parameter identification was carried out using the frequency domain Least Squares Complex Exponential (LSCE) method implemented in the LMS Test.Lab software. Modal analysis results show that the posture dependent modes of the Staubli TX200 structure are located below 30Hz, and the modes above 30 Hz are mostly influenced by the wrist structure and therefore are independent of the first three joints' position. Consequently, only the modes below 30 Hz will be discussed in this work. The auto MAC matrices of the identified mode shapes at each posture, along with the shape, frequency, and modal damping of each of the three identified modes in each configuration of the Staubli TX200 are available in Appendix D.

4.5.2 Kuka KR90

Similar EMA testing was conducted on the Kuka KR90 arm to identify its modal properties. Instrumented hammer (Kistler 9722A500) with a rubber tip was used as the excitation method, and the responses were measured simultaneously using three accelerometers installed on the flange in normal (X), and lateral (Y and Z) directions. These directions are parallel to the X, Y, and Z axis of the local frame of the third link of the robot. Because of the high rigidity of the system in the direction normal to the flange, a high-sensitivity accelerometer (Kistler 8776A50M1) was used to measure the response in X direction, and two identical miniature accelerometers (PCB 352C23) were used to measure the responses in Y and Z directions. Implementing the roving hammer technique, impulses were applied at 23 points distributed on the three links of the robot, including the three X, Y, and Z directions on the flange. The excitation points are shown in Fig.4.5. The actuator brakes were released when performing the hammer tests to account for the controller stiffness, however repeating the tests with brakes engaged did not make any tangible differences in the measured FRFs, showing that the stiffness of the controllers are high-enough to be neglected in this analysis.

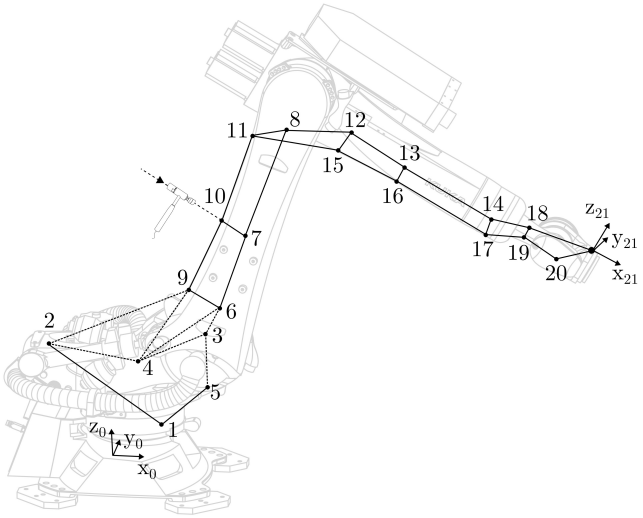

Figure 4.5: Selected nodes and sensors orientation for Kuka KR90.

To study the posture dependent dynamics of the robot structure, EMA was conducted in three different postures. The configurations in which modal testing is carried out on the Kuka KR90 can be found in Table 4.2.

Table 4.2: Modal testing configurations of Kuka KR90.

	Configuration 1	Configuration 2	Configuration 3
q_1	0°	0°	0°
q_2	70°	135°	135°
q_3	−100°	−100°	−140°
q_4	0°	0°	0°
q_5	0°	0°	0°
q_6	0°	0°	0°
	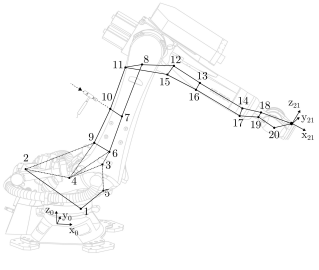	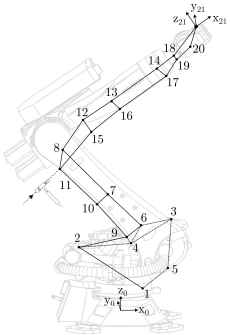	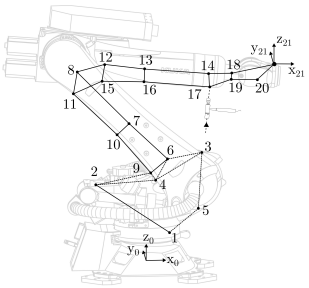

Modal parameter identification was carried out using the frequency domain LSCE method implemented in the LMS Test.Lab software. Similar to Staubli TX200, modal analysis results show that the posture dependent modes of the structure are located below 30Hz, and the modes above 30Hz are mostly influenced by the wrist structure and therefore are independent of the orientation of the first three joints. The modes below 30Hz will be studied for this setup as well. In all postures, four modes are identified below 30Hz. The auto Modal Assurance Criteria (MAC) matrices of the identified mode shapes at each posture, along with the shape, frequency, and modal damping ratio of each of the four identified modes in each configuration are available in Appendix D.

4.6 Joint Identification Results

The joint stiffness and damping parameters (K and C_0) are manually adjusted so that the modal frequency and damping (f_r and ζ_r) obtained from EMA are matching the modal frequency and damping of the model. The modal frequencies and damping ratios obtained from one of the postures are used for the identification of the joint parameters based on Section 4.4.

4.6.1 Staubli TX200

Configuration 1 is used for the joint parameter identification of Staubli TX200 robot. Since only the value for the third rotor inertia is identified in Chapter 3, rotor inertia of the first and second joint are assumed to be proportional to their gear ratios ($I^{zz}_{m_i} = \frac{r_i}{r_3} I^{zz}_{m_3}$). The joint parameters will be manually adjusted in order to have the modal frequencies and damping ratios of the model matching the resulting modal frequencies and damping ratios from EMA. The identified joint parameters are shown in Table 4.3. The higher stiffness value of the second joint with respect to the other joints can be due to design considerations, or the effect of gravity compensation mechanism which is acting as a parallel spring for the second joint.

Table 4.3: Identified joint parameters for Staubli TX200.

Joint	Parameter	Value $10^6 \ \frac{N \cdot m}{rad}$	Parameter	Value $10^3 \ \frac{N \cdot m \cdot sec}{rad}$
1	K_1	1.95	C_1	3.3
2	K_2	5.63	C_2	0.3
3	K_3	1.13	C_3	1.0

The identified and predicted natural frequencies and modal damping ratios for this configuration is available in Table 4.5. Predicted natural frequencies and modal damping ratios are calculated by using the identified joint parameters in Equation4.12. The comparison of experimental and predicted FRFs of the TCP in Cartesian space are presented in Figure 4.6. The predicted FRFs are calculated by using the identified joint parameter values in Equation 4.8. The reason for the missing peak at 12.2Hz in experimental measurements on the second column of Figure 4.6 might be poor excitation quality in Y direction.

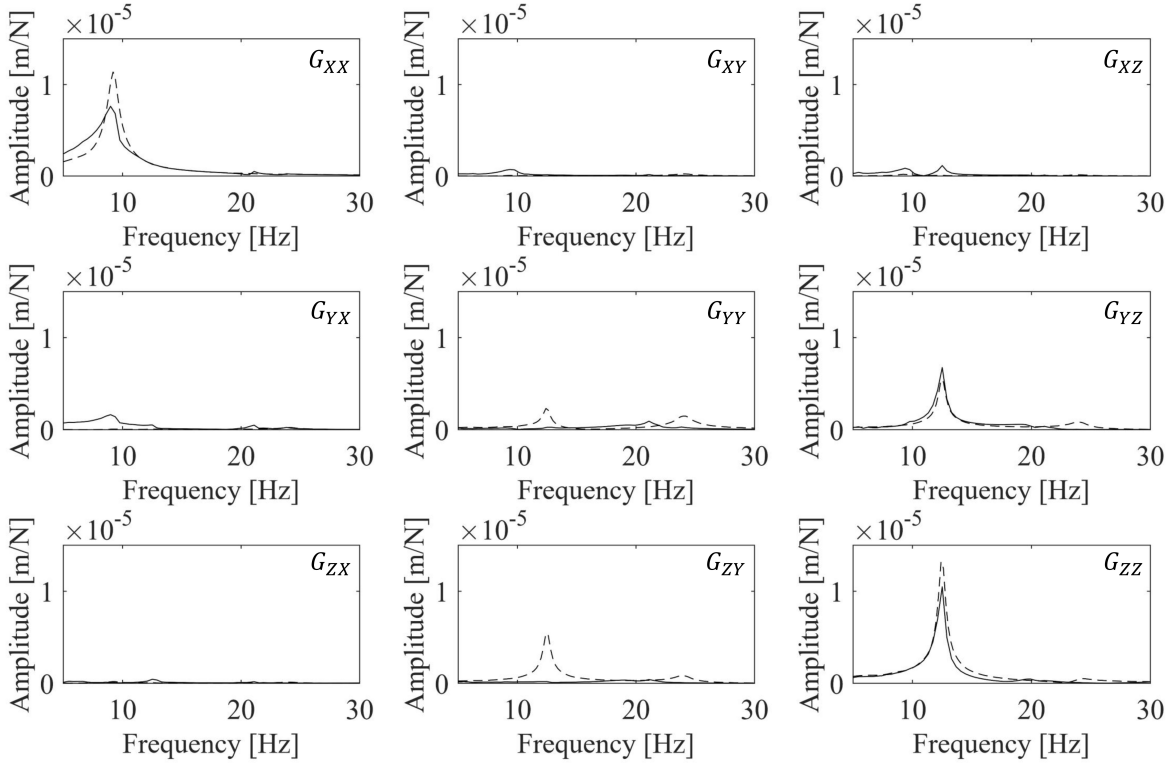

Figure 4.6: Amplitude of measured (——) and predicted (- - -) FRF for TCP of the Staubli TX200 (Configuration 1)

The MAC matrix in Figure 4.7 shows the correlation between identified and predicted mode-shapes, which is obtained by using measured and predicted mode-shape vectors in Equation 4.14. High correlation between the measured and predicted mode-shapes can be seen in this figure.

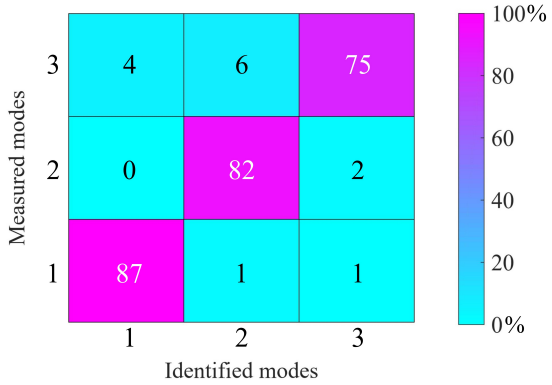

Figure 4.7: MAC matrix of the Staubli TX200 identified model for Configuration 1.

4.6.2 Kuka KR90

Similar to Staubli TX200, the Kuka KR90 joint parameters are identified by using the EMA results for configuration 1. The joint parameters will be identified by fitting the modal frequencies and damping ratios of the model to the ones resulting from EMA. While EMA resulted in four identified modes in each configuration (see Figure D.4), only three of the identified modes can be captured by the model (The mode at 19.2 Hz is not captured). The joint parameter identification is conducted by fitting the modal frequencies and damping ratios of the captured identified modes (modes 1, 2, and 4) on modal frequencies and damping ratios of the predicted modes. The identified parameters for the Kuka KR90 robot is presented in Table 4.4.

Table 4.4: Identified joint parameters for Kuka KR90.

Joint	Parameter	Value $10^6 \frac{N \cdot m}{rad}$	Parameter	Value $10^3 \frac{N \cdot m \cdot sec}{rad}$
1	K_1	3.12	C_1	1.45
2	K_2	3.75	C_2	1.1
3	K_3	2.98	C_3	0.29

The resulting direct and cross FRFs for node 21 are shown in Figure 4.8. The direct

FRFs show a good agreement except for the mode at 19.2 Hz, which cannot be captured by the SDOF joint model. Identified mode-shape of this mode is shown in Figure D.4a and involves deformation of axis 1 around an axis orthogonal to its rotation axis, which is not included in the SDOF joint model.

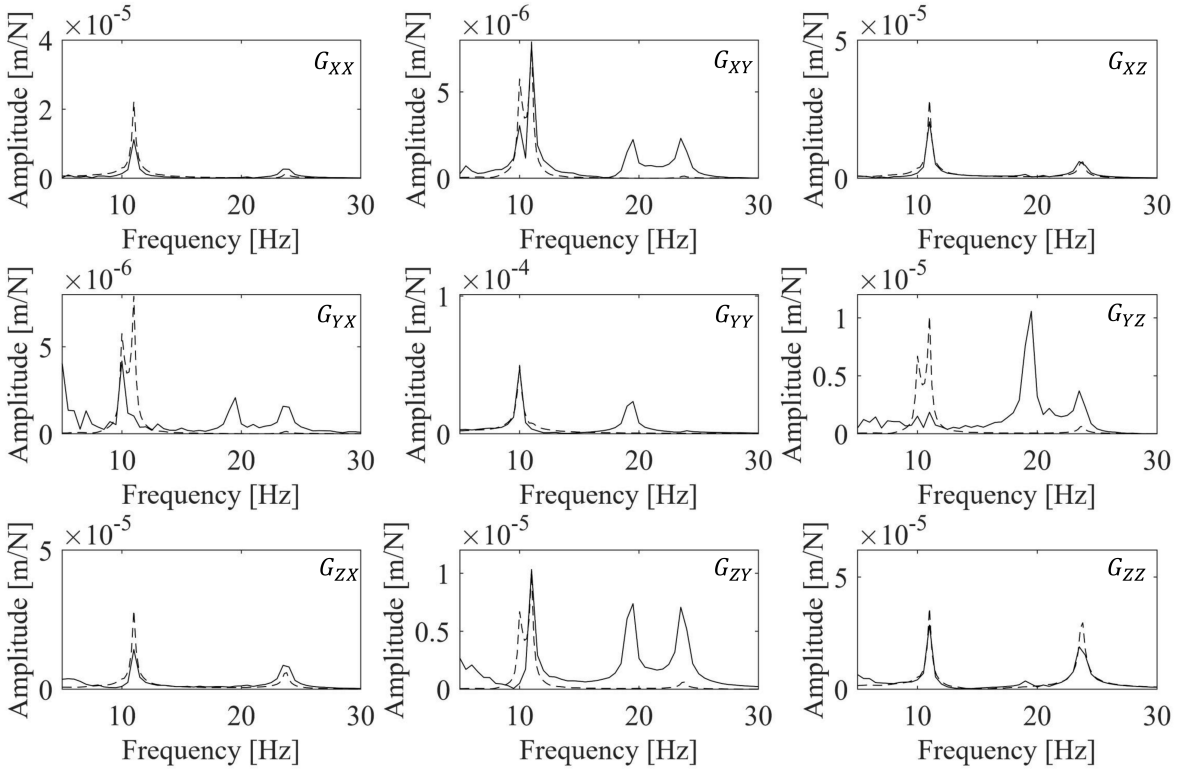

Figure 4.8: Amplitude of measured (——) and predicted (- - -) FRF for the TCP of Kuka KR90 (Configuration 1)

The MAC matrix for this configuration is shown in Figure 4.9, which indicates a close correlation between the identified and predicted mode-shapes. The third measured mode is at 19.2 Hz, which is not captured by the model.

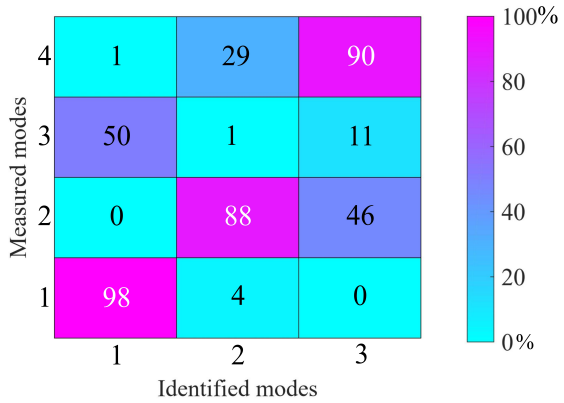

Figure 4.9: MAC matrix of the Kuka KR90 identified model for Configuration 1.

4.7 Verification

4.7.1 Staubli TX200

In order to verify the model performance in predicting dynamic behavior of the system in arbitrary postures, the identified joint parameters, available in Table 4.3, are used along with Equation 4.12 to predict modal parameters of the two remaining Staubli TX200 postures. Table 4.5 shows the comparison between the experimental and modeled natural frequencies and modal damping ratios for all three Staubli TX200 postures.

Table 4.5: Predicted and experimental natural frequencies and damping ratios for all three Staubli TX200 configurations.

Configuration #	Mode shape	$f_r[Hz]$		$\zeta_r[\%]$	
		Exp.	Model	Exp.	Model
Configuration 1		9.200	9.236	4	4.8
		12.43	12.48	1.7	2.2
		23.50	24.03	1.3	2.8
Configuration 2		7.97	7.46	4.07	3.90
		11.293	11.17	1.7	1.66
		25.57	29.19	1.52	4.07
Configuration 3		6.87	8.09	6.51	4.24
		11.73	11.96	2.0	1.97
		24.27	25.42	1.3	3.28

The natural frequencies and damping ratios are predicted with an acceptable error. The average percentage error in natural frequency prediction is 5.47% and the average error in modal damping prediction is 1.1%. Figures 4.10 and 4.11 compare the experimental and modeled FRF at TCP for postures 2 and 3, by using the identified joint parameters and Equation 4.8. The poor excitation quality in Y direction is resulting in the missing peaks in second column of the measured FRFs in both figures. Also, the mode with lowest natural frequency in Figure 4.11 is not predicted properly; this is caused by larger q_5 value in configuration 3 (See Table 4.1), which results in inaccurate prediction of the inertia matrix (M_0) in Equation 4.7.

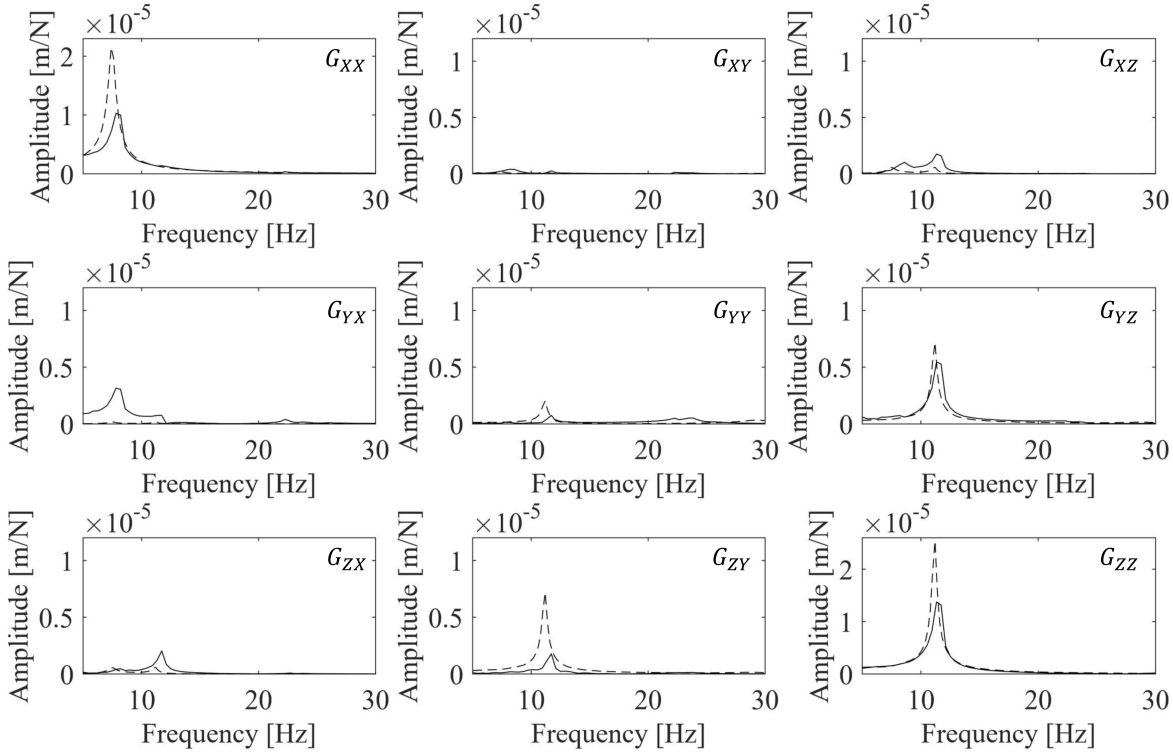

Figure 4.10: Amplitude of measured (——) and modeled (- - -) FRF for the TCP of Staubli TX200 (Configuration 2)

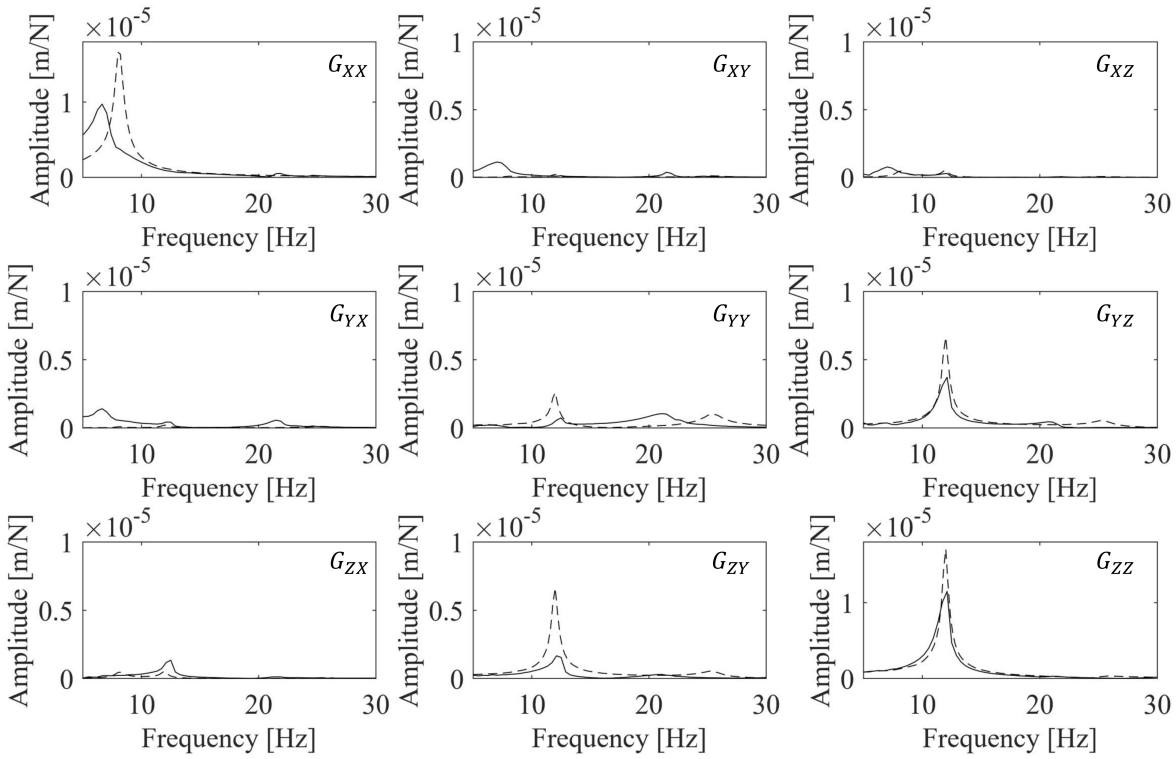

Figure 4.11: Amplitude of measured (——) and modeled (- - -) FRF for the TCP of Staubli TX200 (Configuration 3)

The MAC matrices, showing the correlation between the predicted mode-shapes and identified mode-shapes, for the Staubli TX200 robot in Configurations 2 and 3 are presented in Figure 4.12. Also, the identified mode-shapes for configurations 2 and 3 can be seen in Figure D.2 and D.3. A close correlation is seen in this figure for both postures. The reason for low correlation on the third diagonal element in Figure 4.12b is the large q_5 value (22°), which is not considered in the 3DOF model used in this work (See Table 4.1).

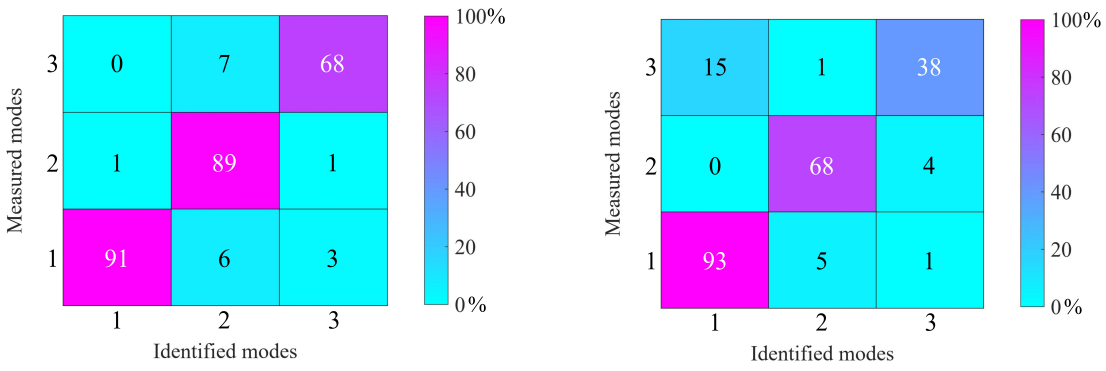

Figure 4.12: Verifying MAC matrix for Staubli TX200 (a) Configuration 2 (b) Configuration 3

4.7.2 Kuka KR90

The identified joint parameters available in Table 4.4 along with Equation 4.12 are used to predict modal parameters of the two remaining Kuka KR90 postures. Table 4.6 shows the comparison between the experimental and modeled natural frequency and modal damping for all three Kuka KR90 postures. The average percentage error in natural frequency prediction is 12.8 % and the average error in damping prediction is 0.28 %.

Table 4.6: Predicted and experimental natural frequency and modal damping for all three Kuka configurations.

Configuration #	Mode shape	$f_n[Hz]$		$\zeta_n[\%]$	
		Exp.	Model	Exp.	Model
Configuration 1		10	10	1.4	1.4
		11	11	1	1
		23.7	23.7	0.8	0.8
Configuration 2		20.4	14.6	1.6	2.1
		11.8	10.9	0.7	1
		25.4	23.7	0.7	0.8
Configuration 3		17.8	14.2	1.2	2
		14.5	13	0.8	1.3
		22.5	21.7	1	0.7

The MAC matrices, presenting the correlation between the three predicted mode shapes and four identified mode shapes, for the Kuka KR90 robot in Configurations 2 and 3 are shown in Figure 4.13. In Configuration 2 (Figure 4.13a), a high level of correlation is observed between the three predicted modes and measured modes two to four (The first identified

mode cannot be captured). In Configuration 3 (Figure 4.13b), although the second and third predicted modes are highly correlated with the third and fourth measured modes, the first predicted mode is not correlated with any of the measured mode-shapes. As shown in Figure D.6a, the difference between the frequencies of the first two identified modes is less than the resolution of measured FRFs (0.5 Hz); as a result, the identified mode shapes of these two modes are highly affected by measurement and identification errors.

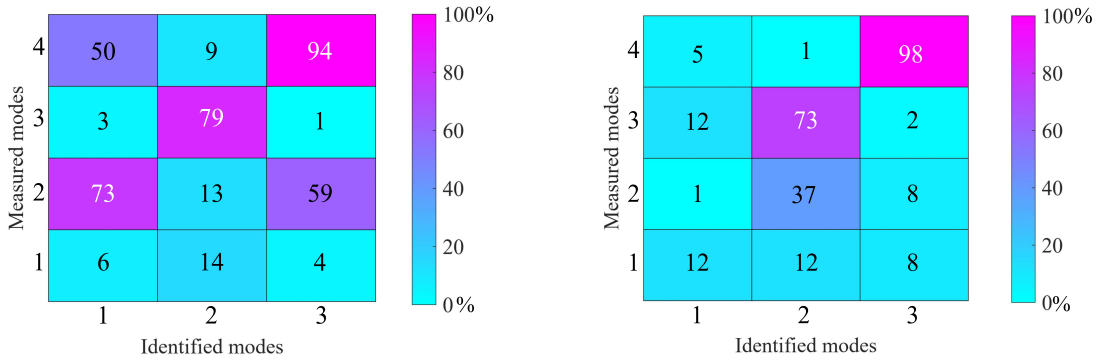

Figure 4.13: Verifying MAC matrix for Kuka KR90 (a) Configuration 2 (b) Configuration 3

4.8 Robotic Milling Stability

To study the stability of robotic milling process, both robot dynamics and milling process dynamics must be studied. Since the prediction of robot dynamic response is already studied in this work, this section will briefly study the milling process dynamic to predict stability limits in robotic milling.

4.8.1 Regenerative Chatter

Figure 4.14 describes the chip formation process during the milling operation. The current tooth is cutting a wavy surface left from previous tooth ($r(t-\tau)$) and leaves a new wavy surface ($r(t)$) to be cut by the next tooth. As a result, the overall chip thickness ($h(t)$) consists of static chip thickness (h_0) and dynamic chip thickness ($\Delta r(t) = r(t) - r(t-\tau)$). While the static chip thickness results in forced vibrations, the dynamic chip thickness results in regenerative chatter, which is the main cause of instability in milling process.

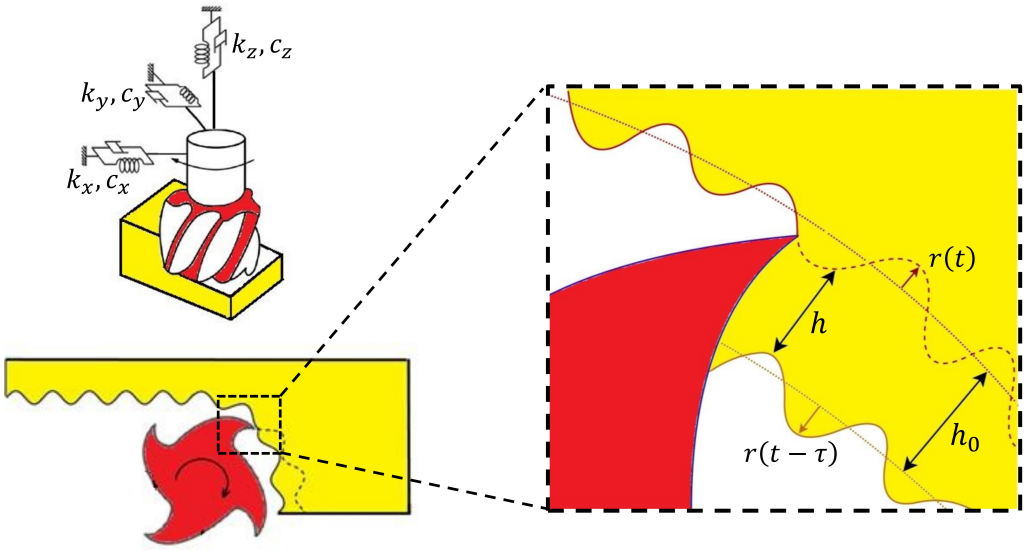

Figure 4.14: Chip formation for milling operation

By neglecting the static chip thickness, the milling regenerative chatter dynamics can be expressed by the closed-loop diagram shown in Figure 4.15, which then can be written in the form of the Delay Differential Equation (DDE) formulated in Equation 4.15.

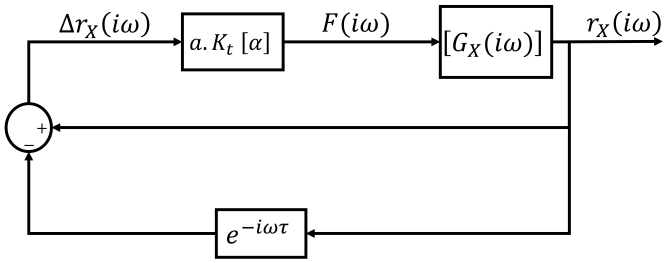

Figure 4.15: Closed-loop diagram presenting dynamics of regenerative chatter

$$M\ddot{r}_X(t) + C\dot{r}_X(t) + Kr_X(t) = aK_t[\alpha(t)]\Delta r_X(t), \tag{4.15}$$

where $M \in \mathbb{R}^{N\times N}$, $C \in \mathbb{R}^{N\times N}$, and $K \in \mathbb{R}^{N\times N}$ are respectively the equivalent mass, damping, and stiffness matrices of the TCP in Cartesian space. The right hand side of this equation shows the cutting force ($F(t) = aK_t[\alpha(t)]\Delta r_X(t)$) where X index stands for being mapped to Cartesian space and a is the axial depth of cut, K_t is the tangential milling force coefficient, and $[\alpha(t)] \in \mathbb{R}^{3\times3}$ is the matrix of the time-periodic directional coefficients, which

is a function of tool angular position (ϕ), number of teeth (N_T), cutting edge angle (γ), radial immersion (b), milling mode (Up-milling/Down-milling), radial cutting force coefficient (K_r), and axial cutting force coefficient (K_a). Figure 4.16 shows the three dimensional milling force model. For more information on definition of $[\alpha(t)]$ and stability of Equation 4.15 refer to[7].

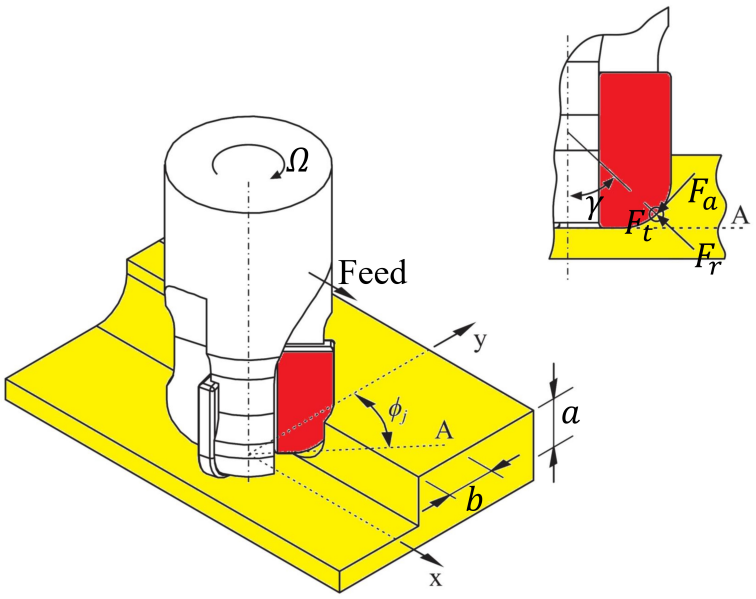

Figure 4.16: Three dimensional milling force model

By transferring the DDE in Equation 4.15 to the frequency domain while considering the average component of the Fourier series expansion of $[\alpha(t)]$ in a tooth passing period (τ) one can have[7]:

$$\{F(i\omega)\} = \frac{N_T}{4\pi} a K_t [\alpha_0](1 - e^{-i\omega_c \tau})[G_X(i\omega)]\{F(i\omega)\}, \tag{4.16}$$

where $G_X(i\omega)$ shows the TCP transfer function identified at the cutter-workpiece contact zone, τ is the tooth passing period, ω_c is the chatter frequency and,

$$[\alpha_0] = \frac{1}{\tau} \int_0^{\tau} [\alpha(t)] dt. \tag{4.17}$$

Equation 4.17 is based on the Zero Order Analysis (ZOA) assumption, which could be found in[7, 6]. By following the work presented by Altintas[7], stability limits are known as a

function of depth of cut (a) and spindle speed (n).

$$a = -\frac{2\pi\Lambda_R}{N_T K_t}\left(1+\kappa^2\right), \tag{4.18}$$

$$n = \frac{60}{N_T\tau} \quad ; \quad \tau = \frac{1}{\omega_c}(\pi - 2\psi + 2k\pi). \tag{4.19}$$

Here, $\psi = tan^{-}1(\kappa)$ is the phase of Λ ($\Lambda = -\frac{N_T}{4\pi}aK_t(1-e^{i\omega_c\tau}) = \Lambda_R + i\Lambda_I$) and k is the integer number of full vibration waves imprinted on the cut arc. Anywhere below the stability limits is known as the stable region, in which the transient vibrations die out due to damping of the system; while lying in the unstable region results in regenerative chatter, which can lead to damages to the system.

4.8.2 Case study

By assuming the TCP is located at the sensor position for experimental setups, and by using the predicted and experimental FRFs, milling stability lobes for different postures are plotted. Table 4.7 shows the milling parameters used to plot stability lobes for this case study.

Table 4.7: Selected milling parameters

Definition	Parameter	Value
Tangential cutting force coefficient	K_t	$800MPa$
Radial cutting force coefficient	K_r	$160MPa$
Axial cutting force coefficient	K_a	$40MPa$
Cutting-edge angle	γ	$40°$
Tool Diameter	D	$10mm$
Number of teeth	N_T	4
Radial immersion	b	$\frac{D}{2}$
Milling mode	$Up/Down$	$Up-milling$

Figure 4.17 compares the stability lobes generated based on experimental and predicted FRFs for Staubli TX200 robot in configurations 1 and 2. Below the stability limits, the self-exciting vibrations will be damped out, which results in stable machining condition, and anywhere above this limit describes the unstable machining conditions. Effect of posture

dependant dynamics of robot on milling stability and value of critical depth of cut is clear in this figure.

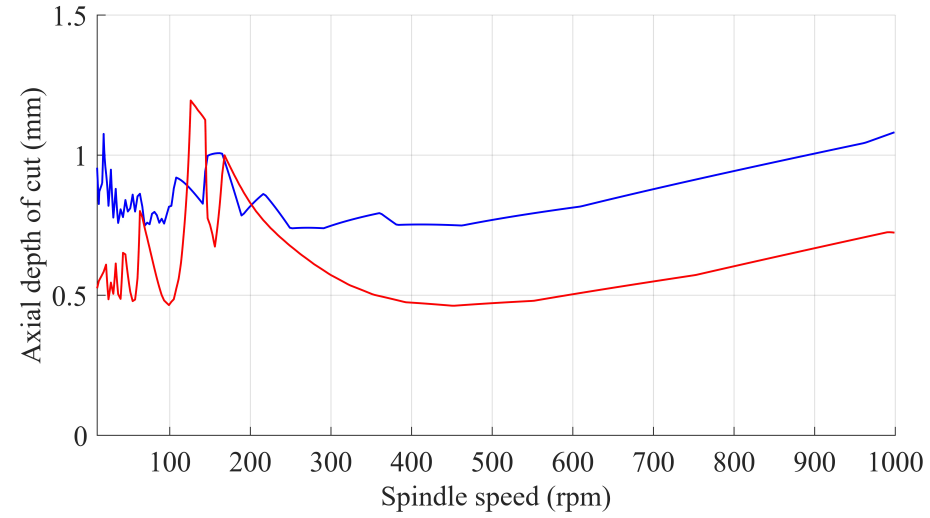

(a)

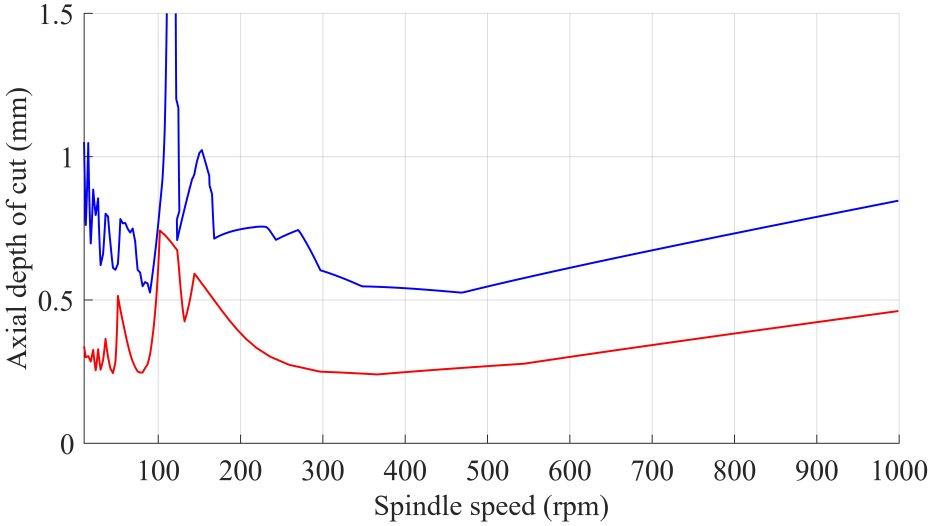

(b)

Figure 4.17: Comparison of calculated stability lobes for Staubli TX200 by using experimental FRF (——) and predicted FRF (——). (a) Configuration 1 (b) Configuration 2

The difference between the two resulting stability diagrams is associated with the error in predicting the associated TCP FRFs, as shown in Fig. 4.6. The difference between the stability lobes in Fig. 4.17 shows that, although the presented MBD model with flexible joints fairly accurately predicts the variation in the robot's modal parameters in various

postures, the prediction error is not acceptable for predicting the stability of the milling process. Further studies must be conducted in order to improve the accuracy of the model and consequently the accuracy of predicting system stability.

Figure 4.18 compares the stability lobes generated based on experimental and predicted FRFs for Kuka KR90 robot in configuration 1, similar trend is observed in Kuka KR90 as well.

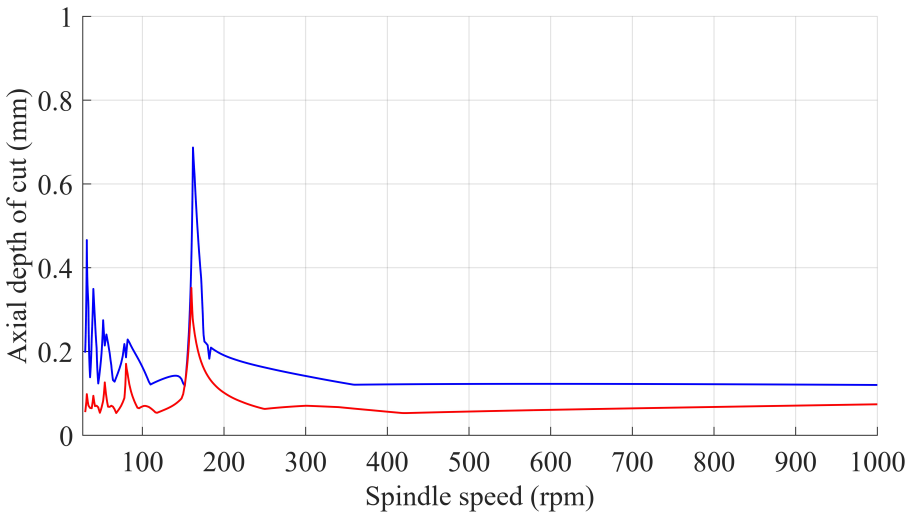

Figure 4.18: Comparison of calculated stability lobes for Kuka KR90 configuration 1 by using experimental FRF (——) and predicted FRF (——).

Chapter 5

Conclusions and Discussion

In this thesis, the MBD modelling and identification of serial robotic systems with SDOF flexible joint model was presented to predict stability of vibrations in robotic machining. The dynamic parameters of the model were identified using a combination of the rigid body model identification method and EMA. The presented model can be used to predict the posture dependent dynamics of the robot, which is essential for planning machining operations to avoid excessive vibrations and chatter. The presented identification approach is convenient to perform in industrial setups and does not require a detailed model of the link geometry. Although the implementation was carried out by considering only the first three degrees of freedom, all the derivations are carried out based on a general N DOF serial robot. Kuka KR90 and Staubli TX200 robotic arms were used as case studies to verify results of this work.

It was shown that the presented MBD model with rigid joints can accurately predict input torque for the system while the robots are moving on arbitrary trajectories. Also the MBD model with SDOF flexible joints can fairly simulate the modal parameters, TCP FRF, and the vibration mode-shapes in various postures accurately. While one mode shape of Kuka KR90 that involved joint deflections around an axis perpendicular to the joint rotation axis could not be simulated using the presented model, the most flexible modes are accurately predicted for the two experimental setups.

Summary

The following is the summary of the modelling approach in this work:

- Dynamic modelling and identification of N DOF serial robots is described based on

the RLRJ model. Identified dynamic parameters are used to predict input torque for arbitrary trajectories.

- The identified dynamic parameters are employed, while using the linearized RLFJ model which assumes lumped linear rotational flexibility around joint axis, to model robot structural dynamics.

- The TCP FRF in Cartesian space is formulated by using the linearized RLFJ model. A frequency domain method is used to predict input-output relationship (FRF) between any two points of the robot structure in Cartesian space.

- Joint parameter identification is conducted by matching natural frequencies and modal damping ratios of the model and the experimental setups. Results are validated by comparing measured and predicted vibration mode-shapes of Staubli TX200 and Kuka KR90 robots in different postures.

Potential Future Research Topics

- **Robot dynamic parameter identification based on the RLFJ model with nonlinear joint behavior.**
  The dynamic parameter identification model presented in Chapter 3 is not considering drives' nonlinearity and joints' flexibility. In addition, path tracking performance of the robots is based on an ideal kinematic description. In reality, the path tracking accuracy of the manipulator is compromised by joints flexibility, kinematic errors, drives' nonlinearity and disturbance forces. By modifying the RLFJ model, to include nonlinear behavior of the joints, higher precision can be achieved.

- **Modelling Joints with Multiple Degrees Of Freedom (MDOF)**
  Although the joints are most flexible around their rotation axis, EMA results show presence of flexible modes due to joints flexibility around orthogonal axes. This could be added to the model to predict modes which are not captured with the model described in this work.

- **Revised EMA testing**
  Although the EMA tests are conducted with utmost attention in this work, poor impulse direction accuracy and low frequency resolution is introducing large errors in the measured modal parameters and mode-shapes, specially when closely spaced modes

are involved. By using a shaker as the input source, along with employing multiple accelerometers (or performing roving sensor modal analysis), this problem could be solved.

- **Milling forces model**
  Due to higher flexibility of robotic machining systems compared to CNC machines, specially in the tool axial direction, milling force models should be updated.

Bibliography

[1] Farzaneh Abdollahi, Heidar A Talebi, and Rajnikant V Patel. A stable neural network-based observer with application to flexible-joint manipulators. *IEEE Transactions on Neural Networks*, 17(1):118–129, 2006.

[2] E. Abele, M. Weigold, and S. Rothenbcher. Modeling and identification of an industrial robot for machining applications. *CIRP Annals*, 56(1):387 – 390, 2007.

[3] Eberhard Abele, Stefan Rothenbücher, and Matthias Weigold. Cartesian compliance model for industrial robots using virtual joints. *Production Engineering*, 2(3):339, 2008.

[4] Alin Albu-Schaffer and Gerd Hirzinger. Parameter identification and passivity based joint control for a 7 dof torque controlled light weight robot. In *Robotics and Automation, 2001. Proceedings 2001 ICRA. IEEE International Conference on*, volume 3, pages 2852–2858. IEEE, 2001.

[5] G. Alici and B. Shirinzadeh. Enhanced stiffness modeling, identification and characterization for robot manipulators. *IEEE Transactions on Robotics*, 21(4):554–564, Aug 2005.

[6] Y Altintaş and E Budak. Analytical prediction of stability lobes in milling. *CIRP Annals-Manufacturing Technology*, 44(1):357–362, 1995.

[7] Yusuf Altintas. Analytical prediction of three dimensional chatter stability in milling. *JSME International Journal Series C Mechanical Systems, Machine Elements and Manufacturing*, 44(3):717–723, 2001.

[8] Yusuf Altintas. *Manufacturing automation: metal cutting mechanics, machine tool vibrations, and CNC design*. Cambridge university press, 2012.

[9] Vigen Arakelian. Gravity compensation in robotics. *Advanced Robotics*, 30(2):79–96, 2016.

[10] Brian Armstrong. On finding exciting trajectories for identification experiments involving systems with nonlinear dynamics. *The International journal of robotics research*, 8(6):28–48, 1989.

[11] Brian Armstrong, Oussama Khatib, and Joel Burdick. The explicit dynamic model and inertial parameters of the puma 560 arm. In *Robotics and Automation. Proceedings. 1986 IEEE International Conference on*, volume 3, pages 510–518. IEEE, 1986.

[12] Karl Johan Åström and Peter Eykhoff. System identificationa survey. *Automatica*, 7(2):123–162, 1971.

[13] Christopher G Atkeson, Chae H An, and John M Hollerbach. Estimation of inertial parameters of manipulator loads and links. *The International Journal of Robotics Research*, 5(3):101–119, 1986.

[14] Stefano Baglioni, Filippo Cianetti, Claudio Braccesi, and Denis Mattia De Micheli. Multibody modelling of n dof robot arm assigned to milling manufacturing. dynamic analysis and position errors evaluation. *Journal of Mechanical Science and Technology*, 30(1):405–420, 2016.

[15] Roger Bernard and S Albright. *Robot calibration*. Springer Science & Business Media, 1993.

[16] Claudiu Bisu, Mehdi Cherif, Alain Gérard, and Jean Yves K'nevez. Dynamic behavior analysis for a six axis industrial machining robot. In *Advanced Materials Research*, volume 423, pages 65–76. Trans Tech Publ, 2012.

[17] Hyouk Ryeol Choi, Wan Kyun Chung, and Youngil Youm. Stiffness analysis and control of redundant manipulators. In *Robotics and Automation, 1994. Proceedings., 1994 IEEE International Conference on*, pages 689–695. IEEE, 1994.

[18] Marcel Cordes and Wolfgang Hintze. Offline simulation of path deviation due to joint compliance and hysteresis for robot machining. *The International Journal of Advanced Manufacturing Technology*, 90(1-4):1075–1083, 2017.

[19] Marcel Cordes, Wolfgang Hintze, and Yusuf Altintas. Chatter stability in robotic milling. *Robotics and Computer-Integrated Manufacturing*, 55:11–18, 2019.

[20] John J Craig. *Introduction to robotics: mechanics and control*, volume 3. Pearson/Prentice Hall Upper Saddle River, NJ, USA:, 2005.

[21] M Da Lio, A Doria, and R Lot. A spatial mechanism for the measurement of the inertia tensor: Theory and experimental results. *Journal of dynamic systems, measurement, and control*, 121(1):111–116, 1999.

[22] J. DePree and C. Gesswein. "robotic machining white paper project", 2008.

[23] Arnaud Devillez and Daniel Dudzinski. Tool vibration detection with eddy current sensors in machining process and computation of stability lobes using fuzzy classifiers. *Mechanical systems and signal processing*, 21(1):441–456, 2007.

[24] Claire Dumas, Stéphane Caro, Sébastien Garnier, and Benoît Furet. Joint stiffness identification of six-revolute industrial serial robots. *Robotics and Computer-Integrated Manufacturing*, 27(4):881–888, 2011.

[25] Selcuk Erkaya. Investigation of joint clearance effects on welding robot manipulators. *Robotics and Computer-Integrated Manufacturing*, 28(4):449–457, 2012.

[26] M Gautier. Optimal motion planning for robot's inertial parameters identification. In *Decision and Control, 1992., Proceedings of the 31st IEEE Conference on*, pages 70–73. IEEE, 1992.

[27] Maxime Gautier, A Janor, and Pierre-Olivier Vandanjon. Didim: A new method for the dynamic identification of robots from only torque data. In *Robotics and Automation, 2008. ICRA 2008. IEEE International Conference on*, pages 2122–2127. IEEE, 2008.

[28] Maxime Gautier and Wisama Khalil. A direct determination of minimum inertial parameters of robots. In *Proceedings. 1988 IEEE International Conference on Robotics and Automation*, pages 1682–1687. IEEE, 1988.

[29] Maxime Gautier and Wisama Khalil. Exciting trajectories for the identification of base inertial parameters of robots. *The International journal of robotics research*, 11(4):362–375, 1992.

[30] Fathi Ghorbel, John Y Hung, and Mark W Spong. Adaptive control of flexible-joint manipulators. *IEEE Control Systems Magazine*, 9(7):9–13, 1989.

[31] M Grotjahn, M Daemi, and B Heimann. Friction and rigid body identification of robot dynamics. *International journal of solids and structures*, 38(10-13):1889–1902, 2001.

[32] Sylvain Guegan, Wisama Khalil, and Philippe Lemoine. Identification of the dynamic parameters of the orthoglide. In *Robotics and Automation, 2003. Proceedings. ICRA'03. IEEE International Conference on*, volume 3, pages 3272–3277. IEEE, 2003.

[33] Levent Guvenc and Krishnaswamy Srinivasan. An overview of robot-assisted die and mold polishing with emphasis on process modeling. *Journal of Manufacturing Systems*, 16(1):48, 1997.

[34] James Hearne. Posture dependent vibration resistance of serial robot manipulators to applied oscillating loads. Master's thesis, University of Waterloo, 2010.

[35] C Henninger and P Eberhard. Computation of stability diagrams for milling processes with parallel kinematic machine tools. *Proceedings of the Institution of Mechanical Engineers, Part I: Journal of Systems and Control Engineering*, 223(1):117–129, 2009.

[36] Tien C Hsia. *System identification: least-squares methods*, volume 1. Lexington books Lexington, 1977.

[37] Hoai Nam Huynh, Georges Kouroussis, Olivier Verlinden, and Edouard Riviere. Modal updating of a 6-axis robot for milling application. *Proceeding of the 25th International Congress on Sound and Vibration*, 2018.

[38] I. Iglesias, M.A. Sebastin, and J.E. Ares. Overview of the state of robotic machining: Current situation and future potential. *Procedia Engineering*, 132:911 – 917, 2015. MESIC Manufacturing Engineering Society International Conference 2015.

[39] H Kazerooni. Automated robotic deburring using impedance control. *IEEE Control Systems Magazine*, 8(1):21–25, 1988.

[40] Christopher W Kennedy and Jaydev P Desai. Modeling and control of the mitsubishi pa-10 robot arm harmonic drive system. *IEEE/ASME Transactions on mechatronics*, 10(3):263–274, 2005.

[41] Wisama Khalil and Etienne Dombre. *Modeling, identification and control of robots*. Butterworth-Heinemann, 2004.

[42] Khashayar Khorasani. Adaptive control of flexible-joint robots. *IEEE Transactions on Robotics and Automation*, 8(2):250–267, 1992.

[43] Alexandr Klimchik, Alexandre Ambiehl, Sébastien Garnier, Benoit Furet, and Anatol Pashkevich. Efficiency evaluation of robots in machining applications using industrial performance measure. *Robotics and Computer-Integrated Manufacturing*, 48:12–29, 2017.

[44] Alexandr Klimchik, Dmitry Bondarenko, Anatol Pashkevich, Sébastien Briot, and Benoît Furet. *Compliance Error Compensation in Robotic-Based Milling*, pages 197–216. Springer International Publishing, Cham, 2014.

[45] Alexandr Klimchik, Stéphane Caro, Yier Wu, Damien Chablat, Benoît Furet, and Anatol Pashkevich. Stiffness modeling of robotic manipulator with gravity compensator. In *Computational Kinematics*, pages 185–192. Springer, 2014.

[46] Alexandr Klimchik, Anatoly Pashkevich, Stéphane Caro, and Benoît Furet. Calibration of industrial robots with pneumatic gravity compensators. In *2017 IEEE International Conference on Advanced Intelligent Mechatronics (AIM)*, pages 285–290. IEEE, 2017.

[47] Alexandr Klimchik, Yier Wu, Stéphane Caro, Claire Dumas, Benoît Furet, and Anatol Pashkevich. Modelling of the gravity compensators in robotic manufacturing cells. *arXiv preprint arXiv:1311.6674*, 2013.

[48] Krzysztof R Kozlowski. *Modelling and identification in robotics*. Springer Science & Business Media, 2012.

[49] Marco Leonesio, Enrico Villagrossi, Manuel Beschi, Alberto Marini, Giacomo Bianchi, Nicola Pedrocchi, Lorenzo Molinari Tosatti, Vladimir Grechishnikov, Yuriy Ilyukhin, and Alexander Isaev. Vibration analysis of robotic milling tasks. *Procedia CIRP*, 67(1):262–267, 2018.

[50] Jing Li, Biao Li, NanYan Shen, Hui Qian, and ZiMeng Guo. Effect of the cutter path and the workpiece clamping position on the stability of the robotic milling system. *The International Journal of Advanced Manufacturing Technology*, 89(9-12):2919–2933, 2017.

[51] Yang Lin, Huan Zhao, and Han Ding. Posture optimization methodology of 6r industrial robots for machining using performance evaluation indexes. *Robotics and Computer-Integrated Manufacturing*, 48:59–72, 2017.

[52] Lennart Ljung. System identification. In *Signal analysis and prediction*, pages 163–173. Springer, 1998.

[53] Ziren Lu, Karunakar B Shimoga, and Andrew A Goldenberg. Experimental determination of dynamic parameters of robotic arms. *Journal of robotic systems*, 10(8):1009–1029, 1993.

[54] Nuno Manuel Mendes Maia and Júlio Martins Montalvao e Silva. *Theoretical and experimental modal analysis*. Research Studies Press, 1997.

[55] Hirokazu Mayeda, Koji Yoshida, and Koichi Osuka. Base parameters of manipulator dynamic models. *IEEE Transactions on Robotics and Automation*, 6(3):312–321, 1990.

[56] Seifeddine Mejri, Vincent Gagnol, Thien-Phu Le, Laurent Sabourin, Pascal Ray, and Patrick Paultre. Dynamic characterization of machining robot and stability analysis. *The International Journal of Advanced Manufacturing Technology*, 82(1):351–359, Jan 2016.

[57] H Moradi, F Bakhtiari-Nejad, and MR Movahhedy. Tuneable vibration absorber design to suppress vibrations: an application in boring manufacturing process. *Journal of sound and vibration*, 318(1-2):93–108, 2008.

[58] Said Mousavi, Vincent Gagnol, Belhassen C Bouzgarrou, and Pascal Ray. Stability optimization in robotic milling through the control of functional redundancies. *Robotics and Computer-Integrated Manufacturing*, 50:181–192, 2018.

[59] Adel Olabi, Mohamed Damak, Richard Bearee, Olivier Gibaru, and Stephane Leleu. Improving the accuracy of industrial robots by offline compensation of joints errors. In *Industrial Technology (ICIT), 2012 IEEE International Conference on*, pages 492–497. IEEE, 2012.

[60] Marouene Oueslati, Richard Béarée, Olivier Gibaru, and George Moraru. Improving the dynamic accuracy of elastic industrial robot joint by algebraic identification approach. In *Systems and Computer Science (ICSCS), 2012 1st International Conference on*, pages 1–6. IEEE, 2012.

[61] Zengxi Pan and Hui Zhang. Robotic machining from programming to process control. In *2008 7th World Congress on Intelligent Control and Automation*, pages 553–558, June 2008.

[62] Zengxi Pan, Hui Zhang, Zhenqi Zhu, and Jianjun Wang. Chatter analysis of robotic machining process. *Journal of Materials Processing Technology*, 173(3):301 – 309, 2006.

[63] Anatol Pashkevich, Alexandr Klimchik, and Damien Chablat. Enhanced stiffness modeling of manipulators with passive joints. *Mechanism and machine theory*, 46(5):662–679, 2011.

[64] C Presse and Maxime Gautier. New criteria of exciting trajectories for robot identification. In *Robotics and Automation, 1993. Proceedings., 1993 IEEE International Conference on*, pages 907–912. IEEE, 1993.

[65] Friedrich Pukelsheim. *Optimal design of experiments*, volume 50. siam, 1993.

[66] Arthur E Quaid and Ralph L Hollis. Cooperative 2-dof robots for precision assembly. In *Robotics and Automation, 1996. Proceedings., 1996 IEEE International Conference on*, volume 3, pages 2188–2193. IEEE, 1996.

[67] Katayon Radkhah, Dana Kulic, and Elizabeth Croft. Dynamic parameter identification for the crs a460 robot. In *Intelligent Robots and Systems, 2007. IROS 2007. IEEE/RSJ International Conference on*, pages 3842–3847. IEEE, 2007.

[68] Christian Reinl, Martin Friedmann, Jörg Bauer, Matthias Pischan, E Abele, and O Von Stryk. Model-based off-line compensation of path deviation for industrial robots in milling applications. In *Advanced Intelligent Mechatronics (AIM), 2011 IEEE/ASME International Conference on*, pages 367–372. IEEE, 2011.

[69] Cristian R Rojas, James S Welsh, Graham C Goodwin, and Arie Feuer. Robust optimal experiment design for system identification. *Automatica*, 43(6):993–1008, 2007.

[70] Michael Ruderman, Frank Hoffmann, and Torsten Bertram. Modeling and identification of elastic robot joints with hysteresis and backlash. *IEEE Trans. Industrial Electronics*, 56(10):3840–3847, 2009.

[71] J Kenneth Salisbury. Active stiffness control of a manipulator in cartesian coordinates. In *Decision and Control including the Symposium on Adaptive Processes, 1980 19th IEEE Conference on*, volume 19, pages 95–100. IEEE, 1980.

[72] Wolfgang Seyfferth, AJ Maghzal, and Jorge Angeles. Nonlinear modeling and parameter identification of harmonic drive robotic transmissions. In *Robotics and Automation,*

1995. Proceedings., 1995 IEEE International Conference on, volume 3, pages 3027–3032. IEEE, 1995.

[73] Mark W Spong. Modeling and control of elastic joint robots. *Journal of dynamic systems, measurement, and control*, 109(4):310–318, 1987.

[74] Mark W Spong, Seth Hutchinson, Mathukumalli Vidyasagar, et al. *Robot modeling and control*. 2006.

[75] S-H Suh, I-K Woo, and S-K Noh. Development of an automatic trajectory planning system (atps) for spray painting robots. In *Robotics and Automation, 1991. Proceedings., 1991 IEEE International Conference on*, pages 1948–1955. IEEE, 1991.

[76] Larry M Sweet and Malcolm C Good. Re-definition of the robot motion control problem: Effects of plant dynamics, drive system constraints, and user requirements. In *Decision and Control, 1984. The 23rd IEEE Conference on*, pages 724–732. IEEE, 1984.

[77] Jan Swevers, Chris Ganseman, Dilek Bilgin, Joris De Schutter, and Hendrik Van Brussel. Optimal robot excitation and identification. *IEEE transactions on robotics and automation*, 13(5):730–740, 1997.

[78] Jan Swevers, Chris Ganseman, Joris De Schutter, and Hendrik Van Brussel. Experimental robot identification using optimised periodic trajectories. *Mechanical Systems and Signal Processing*, 10(5):561–577, 1996.

[79] Jan Swevers, Chris Ganseman, Joris De Schutter, and Hendrik Van Brussel. Generation of periodic trajectories for optimal robot excitation. *Journal of manufacturing science and engineering*, 119(4A):611–615, 1997.

[80] Jan Swevers, Walter Verdonck, and Joris De Schutter. Dynamic model identification for industrial robots. *IEEE Control Systems*, 27(5):58–71, 2007.

[81] J Tlusty and M Polacek. The stability of machine tools against self-excited vibrations in machining, 1963. *Proceedings of the ASME International*, 1963.

[82] SA Tobias and W Fishwick. Theory of regenerative machine tool chatter. *The engineer*, 205(7):199–203, 1958.

[83] Enrico Villagrossi. Robot dynamics modelling and control for machining applications. *Dipartimento di Engegneria Meccanica e Industriale, Università degli Studi di Brescia, Brescia*, 2016.

[84] George-Christopher Vosniakos and Elias Matsas. Improving feasibility of robotic milling through robot placement optimisation. *Robotics and Computer-Integrated Manufacturing*, 26(5):517–525, 2010.

[85] Guifeng Wang, Huiyue Dong, Yingjie Guo, and Yinglin Ke. Chatter mechanism and stability analysis of robotic boring. *The International Journal of Advanced Manufacturing Technology*, 91(1-4):411–421, 2017.

[86] Jun Wu, Jinsong Wang, and Zheng You. An overview of dynamic parameter identification of robots. *Robotics and computer-integrated manufacturing*, 26(5):414–419, 2010.

[87] www.fanuc.eu, 2019.

[88] www.kuka.com. Kr 90 r3100 extra ha, 2019.

[89] www.robotecnik.com, 2019.

[90] www.robotics.org, 2019.

[91] www.staubli.com. Staubli tx200 brochure, 2019.

[92] L. Yuan, Z. Pan, D. Ding, S. Sun, and W. Li. A review on chatter in robotic machining process regarding both regenerative and mode coupling mechanism. *IEEE/ASME Transactions on Mechatronics*, 23(5):2240–2251, Oct 2018.

[93] S.H.H. Zargarbashi, Waseem Khan, and Jorge Angeles. Posture optimization in robot-assisted machining operations. *Mechanism and Machine Theory*, 51:74 – 86, 2012.

Appendix A

Formulation of Base parameters

Mayeda et al. [55] proposed that for an N DOF serial manipulator with all rotational joints the number of base parameters is $7N - 4\beta_1$ ($7N - 4\beta_1 - 2$ if the first joint axis is along the gravity vector). Here, β_1 is the number of links connected by joints whose axes are always parallel to the first joint axis.

By using the RLRJ model from Equation 2.1 each DOF will have a total of 10 inertial parameters: m_i, $m_i r_i^x$, $m_i r_i^y$, $m_i r_i^z$, I_i^{xx}, I_i^{xy}, I_i^{xz}, I_i^{yy}, I_i^{yz}, I_i^{zz}. Here m_i is the mass of link i, ${}^i r_i$ is the position of the center of gravity of link i described in link i frame, and ${}^i I_i$ shows the inertia matrix of link i described in link i frame (See Equation A.1).

$$ {}^i l_i = \begin{bmatrix} l_i^x \\ 0 \\ l_i^z \end{bmatrix}, \qquad {}^i r_i = \begin{bmatrix} r_i^x \\ r_i^y \\ r_i^z \end{bmatrix}, \qquad {}^i I_i = \begin{bmatrix} I_i^{xx} & -I_i^{xy} & -I_i^{xz} \\ -I_i^{xy} & I_i^{yy} & -I_i^{yz} \\ -I_i^{xz} & -I_i^{yz} & I_i^{zz} \end{bmatrix}. \tag{A.1} $$

Here, the definition of l_i^x is the same as a_i and l_i^z presents d_i in Table 2.1. Next,

$$ M_i = \sum_{j=1}^{N} m_j, \tag{A.2} $$

$$ {}^i R_i = M_{i+1} {}^i l_i + m_i {}^i r_i = \begin{bmatrix} R_i^x \\ R_i^y \\ R_i^z \end{bmatrix}, \tag{A.3} $$

$$ {}^{i}J_i = {}^{i}I_i + M_{i+1}\left[\begin{bmatrix} & & \\ & \left({}^{i}l_i \cdot {}^{i}l_i\right) & \\ & & \end{bmatrix}\begin{bmatrix}1&0&0\\0&1&0\\0&0&1\end{bmatrix} - {}^{i}l_i {}^{i}l_i{}^{T}\right] = \begin{bmatrix} J_i^{xx} & J_i^{xy} & J_i^{xz} \\ J_i^{xy} & J_i^{yy} & J_i^{yz} \\ J_i^{xz} & J_i^{yz} & J_i^{zz} \end{bmatrix}. \tag{A.4} $$

By grouping N robot joints into K clusters where $\alpha_c (1 \leq c \leq K)$ is the number of the first joint from c_{th} cluster which its axis is always perpendicular to α_{c-1}. Also β_c is the last joint of the c_{th} cluster where its successor joint (if existent) will be α_{c+1}.

The base parameters of an N DOF robot when the first joint axis is along gravity vector will be found as described in Equation A.5.

$$ \begin{cases} J_i^z + JYB(i) & 1 \leq i \leq N \\ R_i^x & 2 \leq i \leq N \\ R_i^y - RZB(i) & 2 \leq i \leq N \\ J_i^x - J_i^y + JYB(i) & \alpha_2 \leq i \leq N \\ J_i^{xz} + l_i^x RZ(i) & \alpha_2 \leq i \leq N \\ J_i^{xy} + l_i^x RZB(i) & \alpha_2 \leq i \leq N \\ J_i^{yz} + l_i^z RZB(i) & \alpha_2 \leq i \leq N \end{cases}, \tag{A.5} $$

while,

$$ RZ(i) = \begin{cases} 0 & i = \beta_{C(i)} \\ \sum_{j=i+1}^{\beta_{C(i)}} R_j^z & i \neq \beta_{C(i)} \end{cases}, \tag{A.6} $$

$$ RZB(i) = \begin{cases} \sum_{j=\alpha_{C(i)}+1}^{\beta_{C(i)}+1} R_j^z & i = \beta_{C(i)} \ and \ C(i) \neq k \\ 0 & i \neq \beta_{C(i)} \ or \ C(i) = k \end{cases}, \tag{A.7} $$

$$ JYB(i) = \begin{cases} \sum_{j=\alpha_{C(i)}+1}^{\beta_{C(i)}+1} \left(J_j^y + 2 l_j^z RZ(j)\right) & i = \beta_{C(i)} \ and \ C(i) \neq k \\ 0 & i \neq \beta_{C(i)} \ or \ C(i) = k \end{cases}. \tag{A.8} $$

Table A.1: List of base parameters for the 3 DOF robot industrial without motors

Parameter number	Parameter description
1	$I_1^{zz} + I_2^{yy} + I_3^{yy} + (m_2 + m_3)\left(l_1^x\right)^2 + m_3(l_2^x)^2$
2	$I_2^{zz} + m_3(l_2^x)^2$
3	I_3^{zz}
4	$r_2^x m_2 + l_2^x m_3$
5	$r_2^y m_2$
6	$r_3^x m_3$
7	$r_3^y m_3$
8	$I_2^{xx} - I_2^{yy} - m_3(l_2^x)^2$
9	$I_3^{xx} - I_3^{yy}$
10	$I_2^{xz} + r_3^z l_2^x m_3$
11	I_2^{xy}
12	I_2^{yz}
13	I_3^{xz}
14	I_3^{xy}
15	I_3^{yz}

As a result, for the 3 DOF system represented in Figure 2.1 the base parameters are found as shown in Table A.1.

Since the effect of motor inertia could not be neglected in the dynamics of robot, due to high gear ratios, next step is to add the effect of motor inertia to this simplified model to make it more realistic. In order to do so, each DOF will have four additional parameters resulted form considering motor inertial parameters: m_{m_i} is the rotor mass for the i_{th} DOF and ${}^{i}I_{m_i}$ is the inertia matrix of i_{th} DOF rotor;

$$ {}^{i}I_{m_i} = \begin{bmatrix} I_{m_i}^{xx} & 0 & 0 \\ 0 & I_{m_i}^{yy} & 0 \\ 0 & 0 & I_{m_i}^{zz} \end{bmatrix}. \tag{A.9} $$

By adding rotor dynamics to the equations of motion, a total of 42 parameters for the 3 DOF robot are available. Calculating the base parameters show that the updated 3 DOF RLRJ model can be fully expressed using 18 base parameters. These parameters are available in Table A.2.

Table A.2: List of base parameters for the updated 3 DOF model with motors

Parameter number	Parameter description
1	$I_1^{zz} + I_{m_1}^{zz} r_1^2 + I_2^{yy} + I_{m_2}^{yy} + I_3^{yy} + I_{m_3}^{yy}$ $+ (m_2 + m_{m_2} + m_3 + m_{m_3}) (l_1^x)^2 + (m_3 + m_{m_3})(l_2^x)^2$
2	$I_2^{zz} + I_{m_2}^{zz} r_2^2 + (m_3 + m_{m_3})(l_2^x)^2$
3	I_3^{zz}
4	$r_2^x m_2 + l_2^x (m_3 + m_{m_3})$
5	$r_2^y m_2$
6	$r_3^x m_3$
7	$r_3^y m_3$
8	$I_2^{xx} - I_2^{yy} - (m_3 + m_{m_3})(l_2^x)^2$
9	$I_3^{xx} - I_3^{yy}$
10	$I_2^{xz} + r_3^z l_2^x m_3$
11	I_2^{xy}
12	I_2^{yz}
13	I_3^{xz}
14	I_3^{xy}
15	I_3^{yz}
16	$I_{m_3}^{zz}$
17	$I_{m_2}^{xx} - I_{m_2}^{yy}$
18	$I_{m_3}^{xx} - I_{m_3}^{yy}$

Appendix B

Definition of Regressor Matrix

The final regressor matrix used to identify dynamic parameters of the experimental setups ($\Phi_{3\times 27}$) is shown in this section.

$$\Phi(1,1) = \ddot{q}_1$$

$$\Phi(1,2) = 0$$

$$\Phi(1,3) = 2a_1\left(\ddot{q}_1\cos\left(q_2\right) - \dot{q}_1\dot{q}_2\sin\left(q_2\right)\right)$$

$$\Phi(1,4) = -2a_1\left(\ddot{q}_1\sin\left(q_2\right) + \dot{q}_1\dot{q}_2\cos\left(q_2\right)\right)$$

$$\Phi(1,5) = \frac{\ddot{q}_1}{2} - \frac{\ddot{q}_1\cos\left(2q_2\right)}{2} + \dot{q}_1\dot{q}_2\sin\left(2q_2\right)$$

$$\Phi(1,6) = -\cos\left(q_2\right)\dot{q}_2^2 - \ddot{q}_2\sin\left(q_2\right)$$

$$\Phi(1,7) = -\ddot{q}_1\sin\left(2q_2\right) - 2\dot{q}_1\dot{q}_2\cos\left(2q_2\right)$$

$$\Phi(1,8) = \dot{q}_2^2\sin\left(q_2\right) - \ddot{q}_2\cos\left(q_2\right)$$

$$\Phi(1,9) = 0$$

$$\begin{aligned}\Phi(1,10) = {} & a_2\ddot{q}_1\cos(q_3) + a_2\ddot{q}_1\cos(2q_2+q_3) + 2a_1\ddot{q}_1\cos(q_2+q_3) \\ & - 2a_1\dot{q}_1\dot{q}_2\sin(q_2+q_3) - 2a_1\dot{q}_1\dot{q}_3\sin(q_2+q_3) \\ & - a_2\dot{q}_1\dot{q}_3\sin(q_3) - 2a_2\dot{q}_1\dot{q}_2\sin(2q_2+q_3) - a_2\dot{q}_1\dot{q}_3\sin(2q_2+q_3)\end{aligned}$$

$$\begin{aligned}\Phi(1,11) = {} & -a_2\ddot{q}_1\sin(q_3) - a_2\ddot{q}_1\sin(2q_2+q_3) - 2a_1\ddot{q}_1\sin(q_2+q_3) \\ & - 2a_1\dot{q}_1\dot{q}_2\cos(q_2+q_3) - 2a_1\dot{q}_1\dot{q}_3\cos(q_2+q_3) \\ & - a_2\dot{q}_1\dot{q}_3\cos(q_3) - 2a_2\dot{q}_1\dot{q}_2\cos(2q_2+q_3) - a_2\dot{q}_1\dot{q}_3\cos(2q_2+q_3)\end{aligned}$$

$$\Phi(1,12) = \frac{\ddot{q}_1}{2} - \frac{\ddot{q}_1\cos(2q_2+2q_3)}{2} + \dot{q}_1\dot{q}_2\sin(2q_2+2q_3) + \dot{q}_1\dot{q}_3\sin(2q_2+2q_3)$$

$$\begin{aligned}\Phi(1,13) = {} & -\cos(q_2+q_3)\,\dot{q}_2^2 - 2\cos(q_2+q_3)\,\dot{q}_2\dot{q}_3 - \cos(q_2+q_3)\,\dot{q}_3^2 \\ & - \ddot{q}_2\sin(q_2+q_3) - \ddot{q}_3\sin(q_2+q_3)\end{aligned}$$

$$\Phi(1,14) = -\ddot{q}_1\sin(2q_2+2q_3) - 2\dot{q}_1\dot{q}_2\cos(2q_2+2q_3) - 2\dot{q}_1\dot{q}_3\cos(2q_2+2q_3)$$

$$\begin{aligned}\Phi(1,15) = {} & \sin(q_2+q_3)\,\dot{q}_2^2 + 2\sin(q_2+q_3)\,\dot{q}_2\dot{q}_3 + \sin(q_2+q_3)\,\dot{q}_3^2 \\ & - \ddot{q}_2\cos(q_2+q_3) - \ddot{q}_3\cos(q_2+q_3)\end{aligned}$$

$$\Phi(1,16) = 0$$

$$\Phi(1,17) = \frac{\ddot{q}_1}{2} - \frac{\ddot{q}_1\cos(2r_2q_2)}{2} + r_2\dot{q}_1\dot{q}_2\sin(2r_2q_2)$$

$$\begin{aligned}\Phi(1,18) = {} & \frac{\ddot{q}_1}{2} - \frac{\ddot{q}_1\cos(2q_2+2r_3q_3)}{2} + \dot{q}_1\dot{q}_2\sin(2q_2+2r_3q_3) \\ & + r_3\dot{q}_1\dot{q}_3\sin(2q_2+2r_3q_3)\end{aligned}$$

$$\Phi(1,19) = 0$$

$$\Phi(1,20) = 0$$

$$\Phi(1,21) = 0$$

$$\Phi(1,22) = \dot{q}_1$$

$$\Phi(1,23) = sign(\dot{q}_1)$$

$$\Phi(1,24) = 0$$

$$\Phi(1,25) = 0$$

$$\Phi(1,26) = 0$$

$$\Phi(1,27) = 0$$

$$\Phi(2,1) = 0$$

$$\Phi(2,2) = \ddot{q}_2$$

$$\Phi(2,3) = a_1\dot{q}_1^2 \sin(q_2) - g\cos(q_2)$$

$$\Phi(2,4) = a_1 \cos(q_2)\,\dot{q}_1^2 + g\sin(q_2)$$

$$\Phi(2,5) = -\frac{\dot{q}_1^2 \sin(2q_2)}{2}$$

$$\Phi(2,6) = -\ddot{q}_1 \sin(q_2)$$

$$\Phi(2,7) = \dot{q}_1^2 \cos(2q_2)$$

$$\Phi(2,8) = -\ddot{q}_1 \cos(q_2)$$

$$\Phi(2,9) = \ddot{q}_2 + \ddot{q}_3$$

$$\Phi(2,10) = 2a_2\ddot{q}_2\cos(q_3) - g\cos(q_2+q_3) + a_2\ddot{q}_3\cos(q_3) + a_1\dot{q}_1^2\sin(q_2+q_3) - a_2\dot{q}_3^2\sin(q_3) + a_2\dot{q}_1^2\sin(2q_2+q_3) - 2a_2\dot{q}_2\dot{q}_3\sin(q_3)$$

$$\Phi(2,11) = g\sin(q_2+q_3) - 2a_2\ddot{q}_2\sin(q_3) - a_2\ddot{q}_3\sin(q_3) + a_1\dot{q}_1^2\cos(q_2+q_3) - a_2\dot{q}_3^2\cos(q_3) + a_2\dot{q}_1^2\cos(2q_2+q_3) - 2a_2\dot{q}_2\dot{q}_3\cos(q_3)$$

$$\Phi(2,12) = -\frac{\dot{q}_1^2 \sin(2q_2+2q_3)}{2}$$

$$\Phi(2,13) = -\ddot{q}_1 \sin(q_2 + q_3)$$

$$\Phi(2,14) = \dot{q}_1^2 \cos(2q_2 + 2q_3)$$

$$\Phi(2,15) = -\ddot{q}_1 \cos(q_2 + q_3)$$

$$\Phi(2,16) = \ddot{q}_2 + r_3\ddot{q}_3$$

$$\Phi(2,17) = \frac{-r_2\dot{q}_1^2 \sin(2r_2q_2)}{2}$$

$$\Phi(2,18) = \frac{-\dot{q}_1^2 \sin(2q_2 + 2r_3q_3)}{2}$$

$$\Phi(2,19) = -\cos(q_2)$$

$$\Phi(2,20) = -\cos(2q_2)$$

$$\Phi(2,21) = -\cos(3q_2)$$

$$\Phi(2,22) = 0$$

$$\Phi(2,23) = 0$$

$$\Phi(2,24) = \dot{q}_2$$

$$\Phi(2,25) = sign(\dot{q}_2)$$

$$\Phi(2,26) = 0$$

$$\Phi(2,27) = 0$$

$$\Phi(3,1) = 0$$

$$\Phi(3,2) = 0$$

$$\Phi(3,3) = 0$$

$$\Phi(3,4) = 0$$

$$\Phi(3,5) = 0$$

$$\Phi(3,6) = 0$$

$$\Phi(3,7) = 0$$

$$\Phi(3,8) = 0$$

$$\Phi(3,9) = \ddot{q}_2 + \ddot{q}_3$$

$$\Phi(3,10) = a_2\ddot{q}_2\cos(q_3) - g\cos(q_2+q_3) + a_1\dot{q}_1^2\sin(q_2+q_3) + \frac{a_2\dot{q}_1^2\sin(q_3)}{2} + a_2\dot{q}_2^2\sin(q_3) + \frac{a_2\dot{q}_1^2\sin(2q_2+q_3)}{2}$$

$$\Phi(3,11) = g\sin(q_2+q_3) - a_2\ddot{q}_2\sin(q_3) + a_1\dot{q}_1^2\cos(q_2+q_3) + \frac{a_2\dot{q}_1^2\cos(q_3)}{2} + a_2\dot{q}_2^2\cos(q_3) + \frac{a_2\dot{q}_1^2\cos(2q_2+q_3)}{2}$$

$$\Phi(3,12) = -\frac{\dot{q}_1^2\sin(2q_2+2q_3)}{2}$$

$$\Phi(3,13) = -\ddot{q}_1\sin(q_2+q_3)$$

$$\Phi(3,14) = \dot{q}_1^2\cos(2q_2+2q_3)$$

$$\Phi(3,15) = -\ddot{q}_1\cos(q_2+q_3)$$

$$\Phi(3,16) = r_3(\ddot{q}_2 + r_3\ddot{q}_3)$$

$$\Phi(3,17) = 0$$

$$\Phi(3,18) = \frac{-r_3\dot{q}_1^2\sin(2q_2+2r_3q_3)}{2}$$

$$\Phi(3,19) = 0$$

$$\Phi(3,20) = 0$$

$$\Phi(3,21) = 0$$

$$\Phi(3,22) = 0$$

$$\Phi(3,23) = 0$$

$$\Phi(3,24) = 0$$

$$\Phi(3,25) = 0$$

$$\Phi(3,26) = \dot{q_3}$$

$$\Phi(3,27) = sign(\dot{q_3})$$

Appendix C

Supplementary Inertia Identification Results

C.1 Staubli TX200

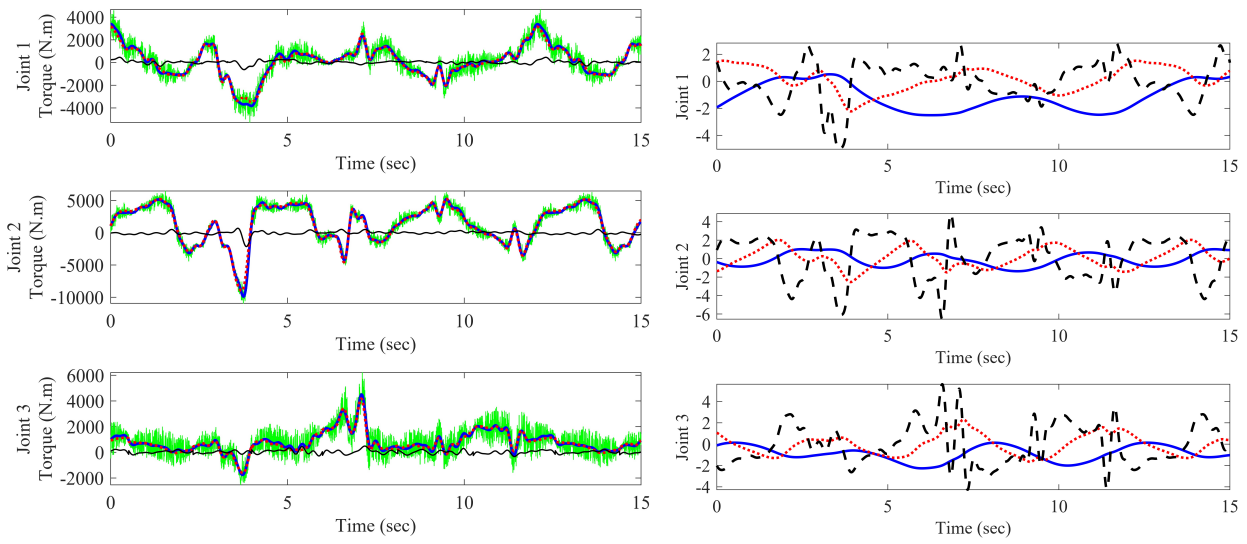

(a) (b)

Figure C.1: (a) Measured and predicted torque of the identification trajectory 1 for Staubli TX200 (Measured torque (——), Filtered torque (——), Predicted torque (- - -), Prediction error (——)).
(b) Joint-space position $[rad]$ (——), Joint-space velocity $[rad/sec]$ (- - -), and Joint-space acceleration $[rad/sec^2]$ (— —) of the identification trajectory 1 for Staubli TX200.

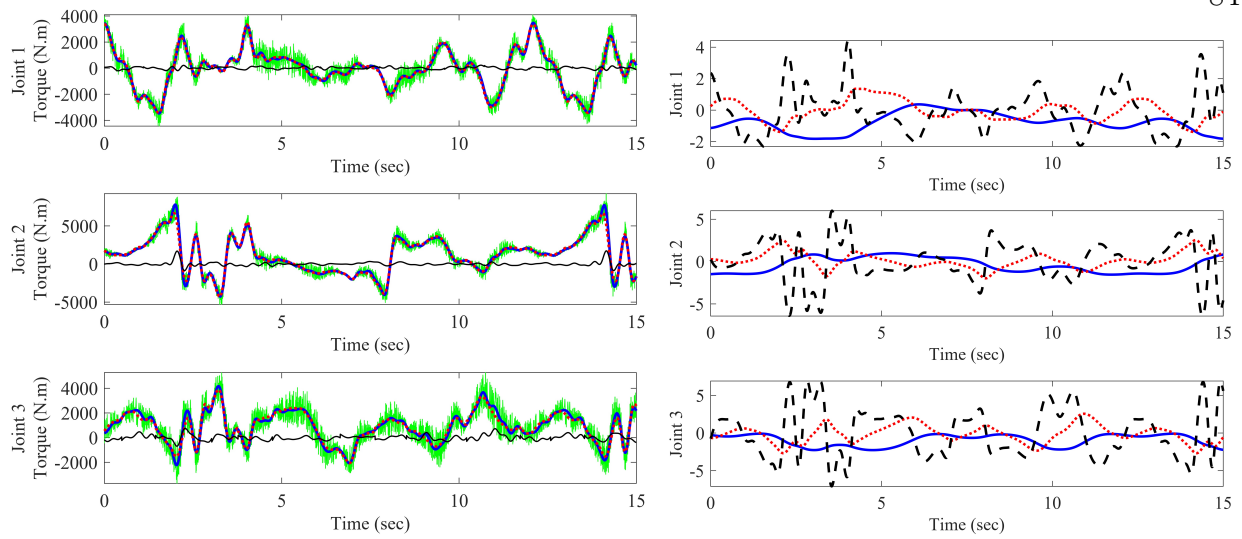

(a) (b)

Figure C.2: (a) Measured and predicted torque of the identification trajectory 2 for Staubli TX200 (Measured torque (——), Filtered torque (——), Predicted torque (- - -), Prediction error (——)).
(b) Joint-space position $[rad]$ (——), Joint-space velocity $[rad/sec]$ (- - -), and Joint-space acceleration $[rad/sec^2]$ (— —) of the identification trajectory 2 for Staubli TX200.

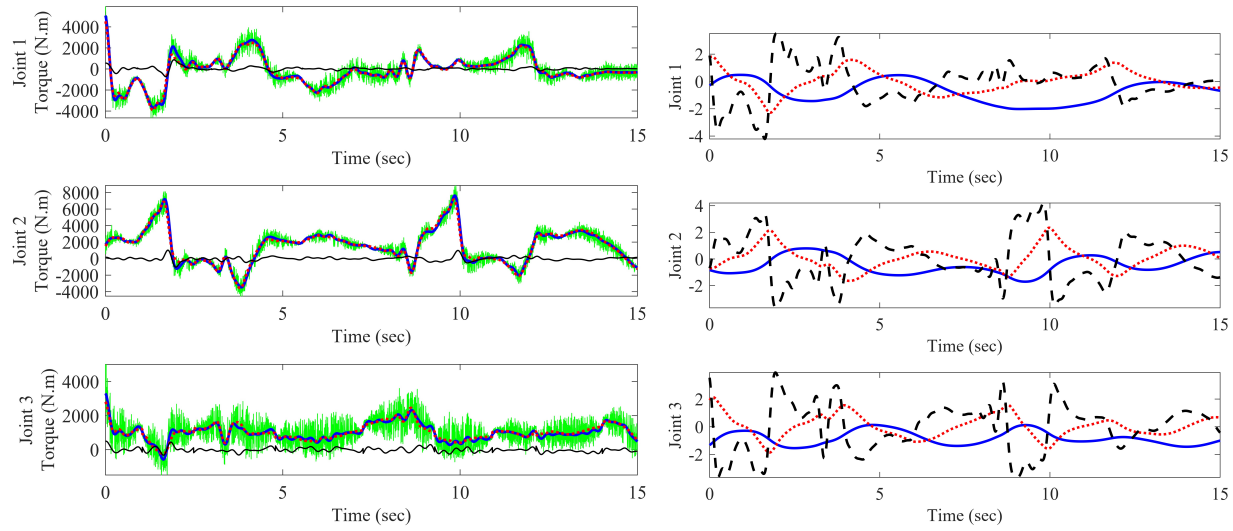

(a) (b)

Figure C.3: (a) Measured and predicted torque of the identification trajectory 3 for Staubli TX200 (Measured torque (——), Filtered torque (——), Predicted torque (- - -), Prediction error (——)).
(b) Joint-space position $[rad]$ (——), Joint-space velocity $[rad/sec]$ (- - -), and Joint-space acceleration $[rad/sec^2]$ (— —) of the identification trajectory 3 for Staubli TX200.

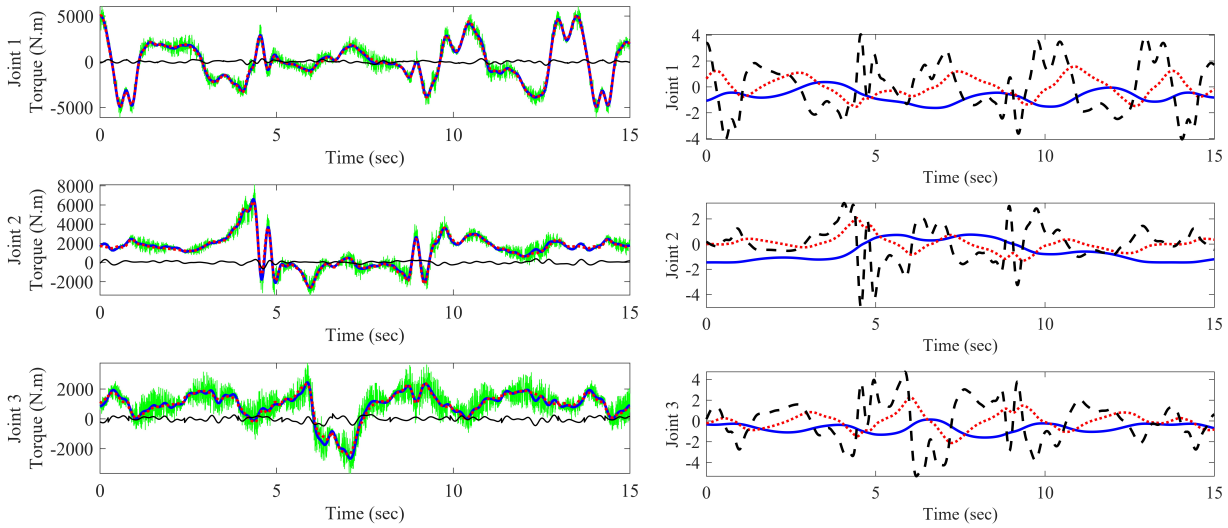

(a) (b)

Figure C.4: (a) Measured and predicted torque of the identification trajectory 4 for Staubli TX200 (Measured torque (——), Filtered torque (——), Predicted torque (- - -), Prediction error (——)).
(b) Joint-space position $[rad]$ (——), Joint-space velocity $[rad/sec]$ (- - -), and Joint-space acceleration $[rad/sec^2]$ (— —) of the identification trajectory 4 for Staubli TX200.

Table C.1: RMS of torque prediction percentage error for Staubli TX200 identification trajectories

	Joint 1	Joint 2	Joint 3
identification trajectory 1	4.6%	0.8%	2.9%
identification trajectory 2	0.6%	3.0%	4.2%
identification trajectory 3	4.6%	1.0%	0.2%
identification trajectory 4	0.1%	0.7%	1.3%

C.2 Kuka KR90

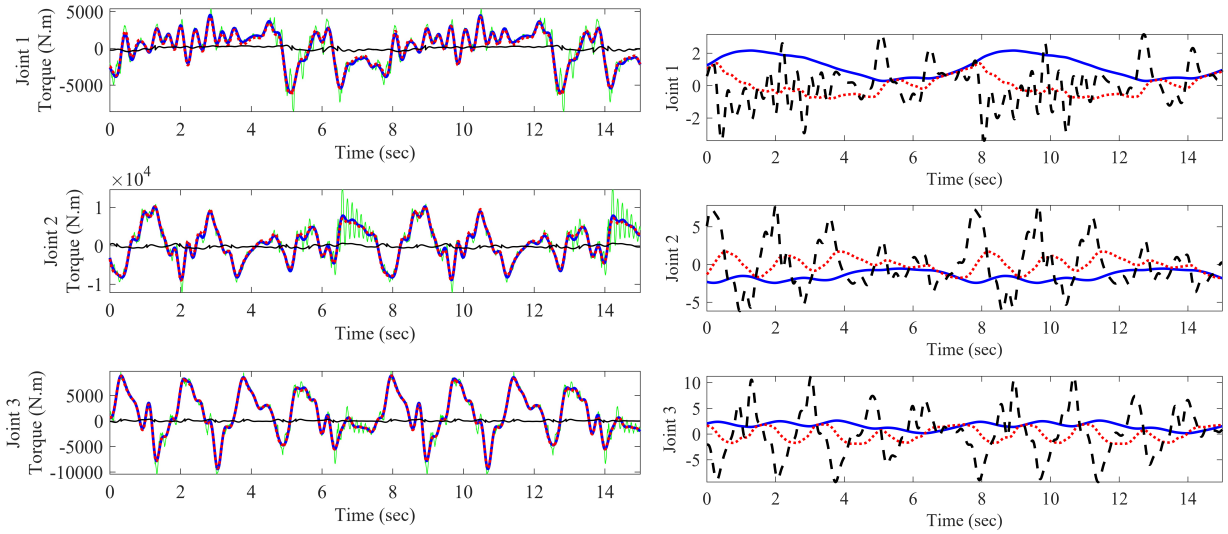

(a) (b)

Figure C.5: (a) Measured and predicted torque of the identification trajectory 1 for Kuka KR90 (Measured torque (——), Filtered torque (——), Predicted torque (- - -), Prediction error (——)).
(b) Joint-space position $[rad]$ (——), Joint-space velocity $[rad/sec]$ (- - -), and Joint-space acceleration $[rad/sec^2]$ (— —) of the identification trajectory 1 for Kuka KR90.

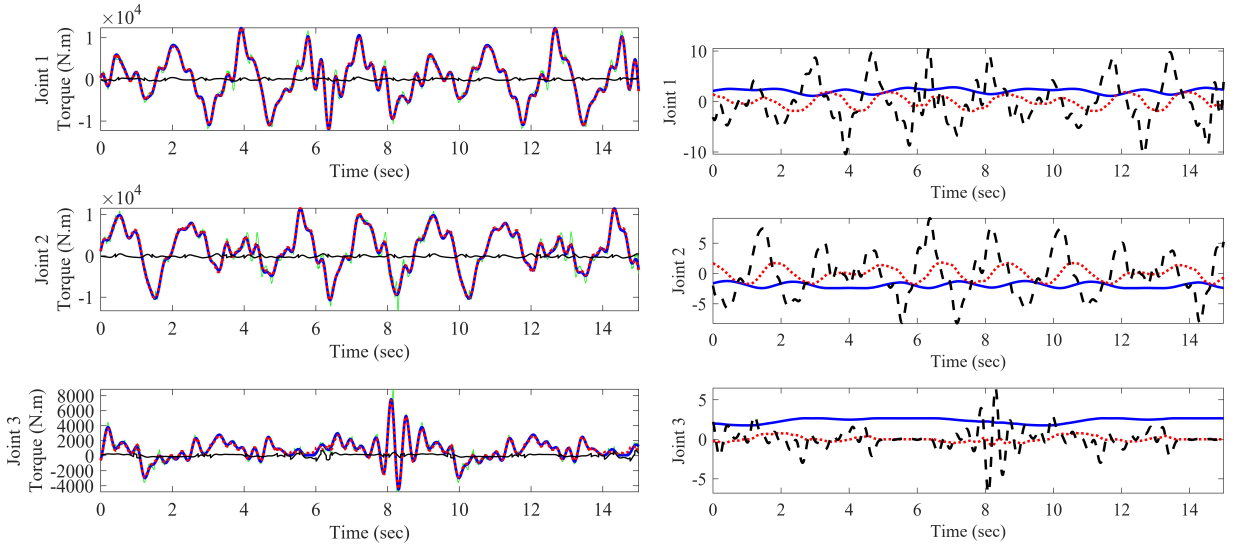

(a) (b)

Figure C.6: (a) Measured and predicted torque of the identification trajectory 2 for Kuka KR90 (Measured torque (——), Filtered torque (——), Predicted torque (- - -), Prediction error (——)).
(b) Joint-space position $[rad]$ (——), Joint-space velocity $[rad/sec]$ (- - -), and Joint-space acceleration $[rad/sec^2]$ (— —) of the identification trajectory 2 for Kuka KR90.

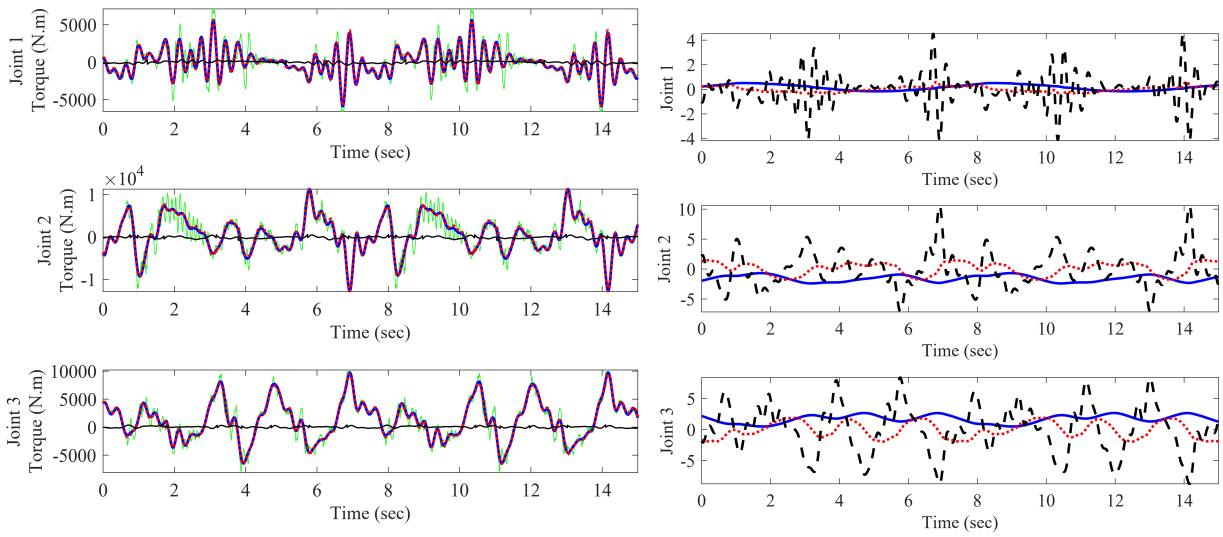

(a) (b)

Figure C.7: (a) Measured and predicted torque of the identification trajectory 3 for Kuka KR90 (Measured torque (——), Filtered torque (——), Predicted torque (- - -), Prediction error (——)).
(b) Joint-space position $[rad]$ (——), Joint-space velocity $[rad/sec]$ (- - -), and Joint-space acceleration $[rad/sec^2]$ (— —) of the identification trajectory 3 for Kuka KR90.

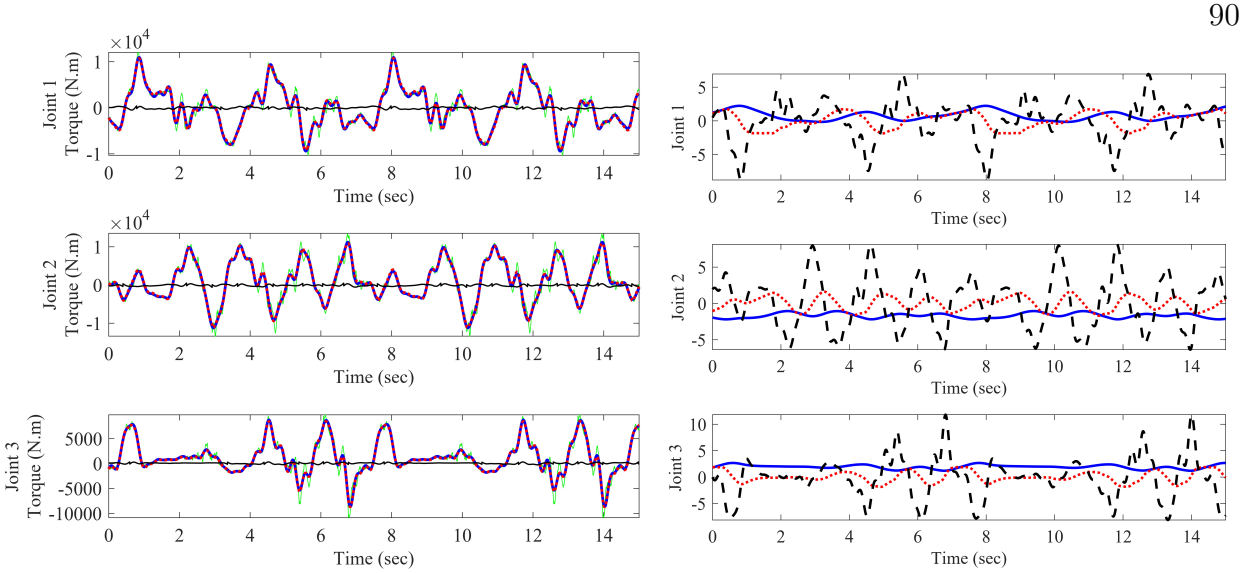

(a) (b)

Figure C.8: (a) Measured and predicted torque of the identification trajectory 4 for Kuka KR90 (Measured torque (——), Filtered torque (——), Predicted torque (- - -), Prediction error (——)).
(b) Joint-space position $[rad]$ (——), Joint-space velocity $[rad/sec]$ (- - -), and Joint-space acceleration $[rad/sec^2]$ (— —) of the identification trajectory 4 for Kuka KR90.

Table C.2: RMS of torque prediction percentage error for KUKA KR90 identification trajectories

	Joint 1	Joint 2	Joint 3
identification trajectory 1	4.1%	0.6%	1.0%
identification trajectory 2	0.4%	0.8%	5.4%
identification trajectory 3	2.2%	0.0%	0.3%
identification trajectory 4	0.4%	0.3%	0.7%

Appendix D

Experimental Modal Analysis Results

D.1 Staubli TX200

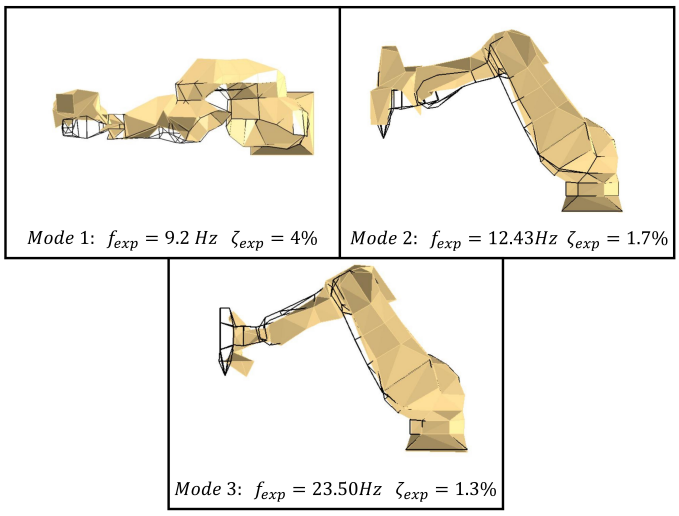

(a)

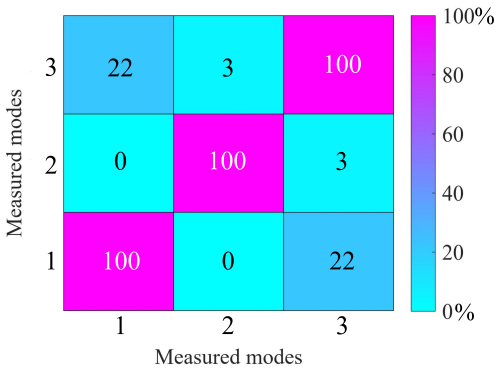

(b)

Figure D.1: (a) Experimental mode shapes (Deformed ( ), Undeformed ( )) for Staubli Tx200 Configuration 1. (b) Corresponding auto-MAC matrix

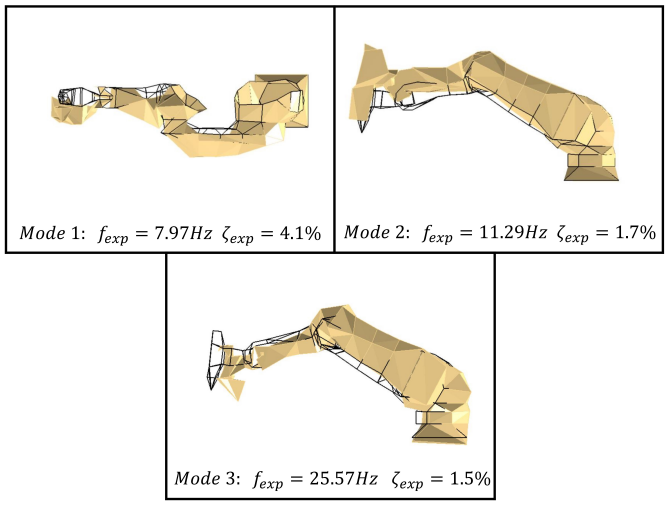

(a)

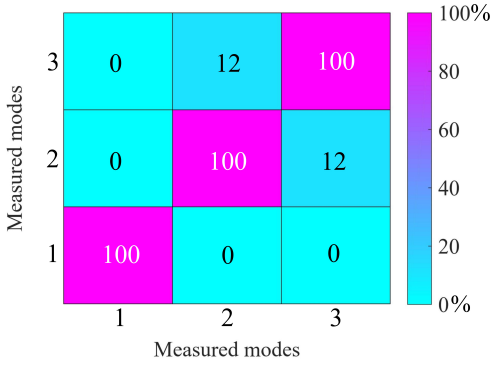

(b)

Figure D.2: (a) Experimental mode shapes (Deformed (■), Undeformed (▬)) for Staubli Tx200 Configuration 2. (b) Corresponding auto-MAC matrix

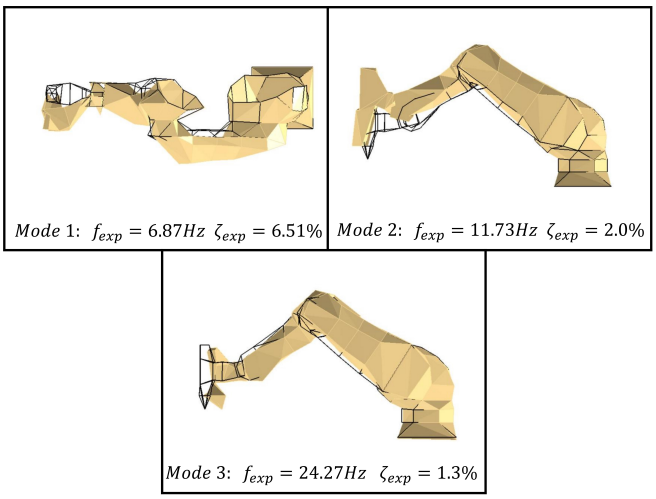

(a)

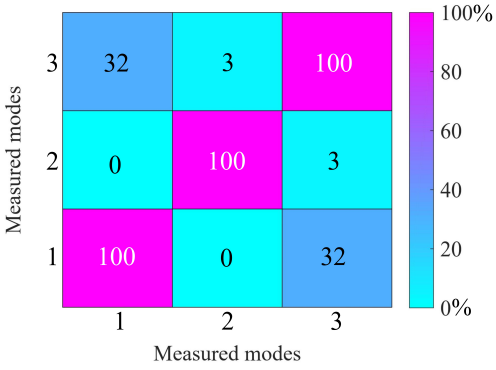

(b)

Figure D.3: (a) Experimental mode shapes (Deformed (■), Undeformed (▬)) for Staubli Tx200 Configuration 3. (b) Corresponding auto-MAC matrix

D.2 Kuka KR90

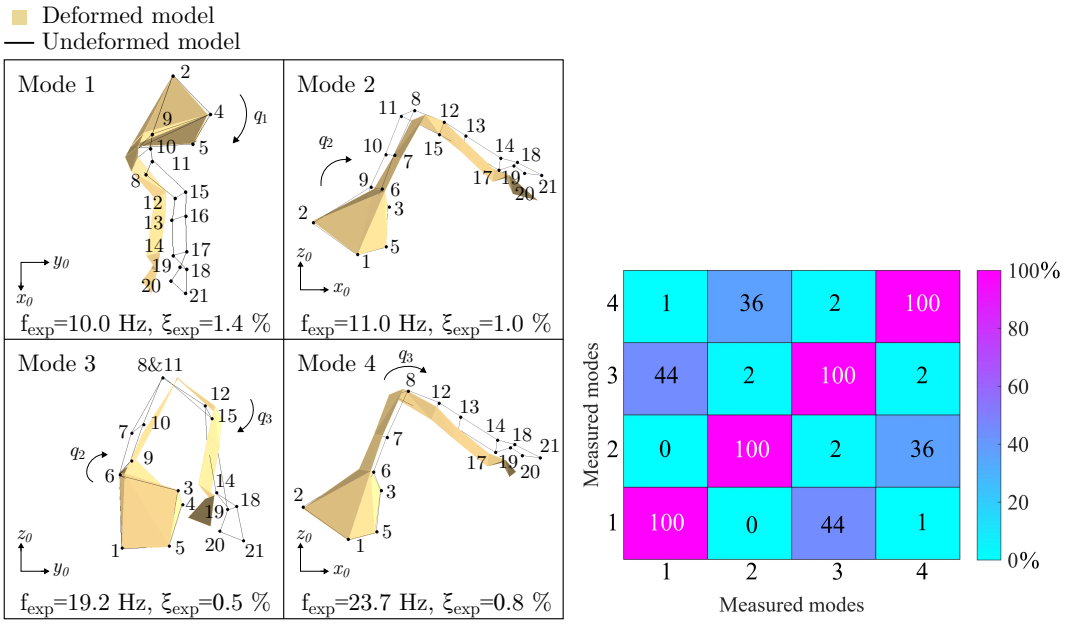

(a) (b)

Figure D.4: (a) Experimental mode shapes (Deformed (■), Undeformed (——)) for Kuka KR90 Configuration 1. (b) Corresponding auto-MAC matrix

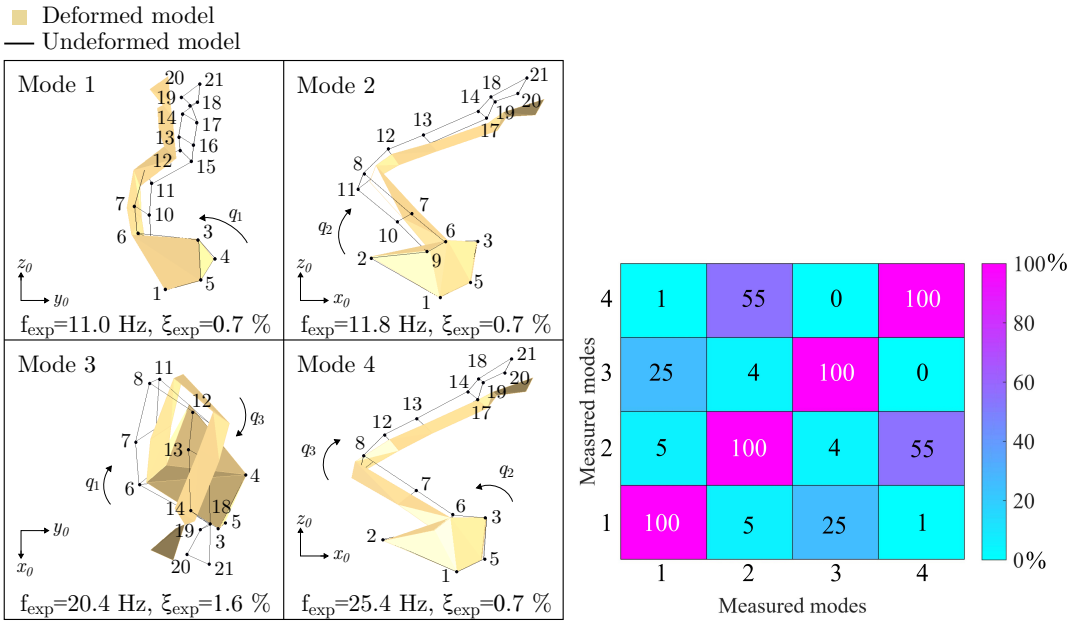

(a) (b)

Figure D.5: (a) Experimental mode shapes (Deformed (■), Undeformed (——)) for Kuka KR90 Configuration 2. (b) Corresponding auto-MAC matrix

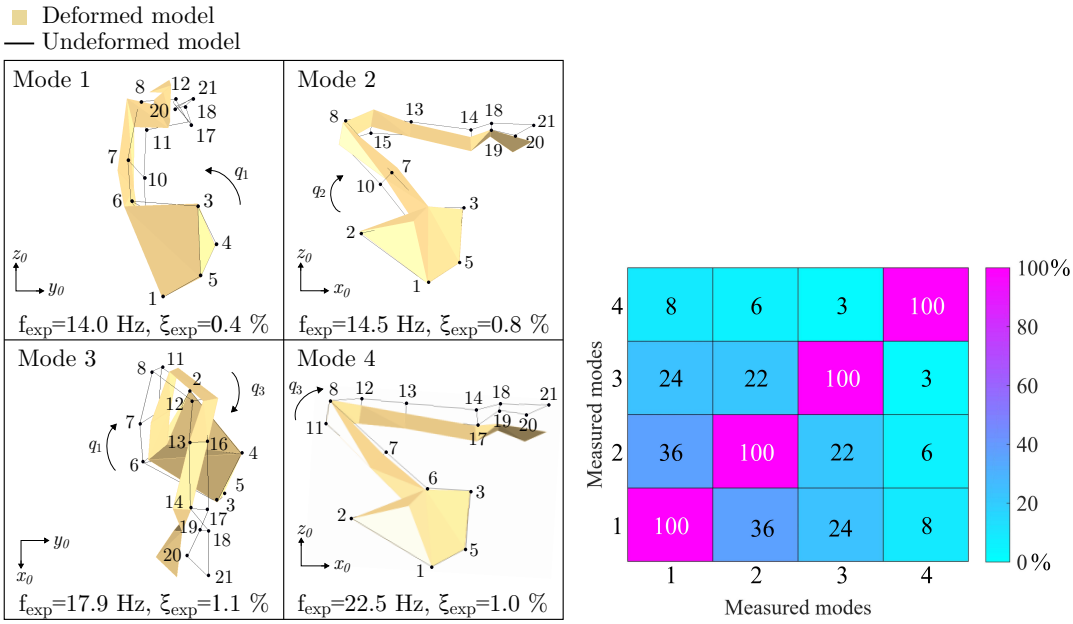

(a) (b)

Figure D.6: (a) Experimental mode shapes (Deformed (■), Undeformed (——)) for Kuka KR90 Configuration 3. (b) Corresponding auto-MAC matrix